Surface and Interface Analysis

WILEY

SURFACE and INTERFACE ANALYSIS

RESEARCH ARTICLE OPEN ACCESS

X-Ray Photoelectron Spectroscopy Analysis of Indium and Indium-Containing Compounds

Jeffrey D. Henderson[1] | Laurel Pearson[1,2] | Heng-Yong Nie[1,3] | Mark C. Biesinger[1,2]

[1]Surface Science Western, The University of Western Ontario, London, Ontario, Canada | [2]Department of Chemistry, The University of Western Ontario, London, Ontario, Canada | [3]Department of Physics, The University of Western Ontario, London, Ontario, Canada

Correspondence: Jeffrey D. Henderson (jhende64@uwo.ca) | Mark C. Biesinger (biesingr@uwo.ca)

Received: 6 May 2024 | **Revised:** 20 August 2024 | **Accepted:** 28 August 2024

Funding: Financial support was provided by the Natural Sciences and Engineering Research Council of Canada (Discovery Grant # RGPIN-2022-04475). The Kratos Axis Supra instrument used in this study was provided as part of a Canada Foundation for Innovation (CFI-IF #35961) and Ontario Research Fund.

Keywords: critical minerals | indium | ITO | time-of-flight secondary mass spectrometry | X-ray photoelectron spectroscopy

ABSTRACT

X-ray photoelectron spectroscopy (XPS) is widely employed across various research fields due to its surface and chemical sensitivity. However, accurate interpretation poses a challenge due to the lack of comprehensive reference data in the literature, leading to misinterpretation, especially among novice users. Analyzing the chemical state of indium and indium-containing compounds is particularly challenging due to subtle shifts in the binding energies of the commonly used 3d core line. This paper presents and discusses a collection of reference data, including the In 3d, In 3p, In 4d, In MNN, and relevant counter ion signals. Additionally, it explores other useful information such as the modified Auger parameter and Wagner (or chemical state) plots. The utility of X-ray–induced Auger electrons is demonstrated in the speciation of mixed systems.

1 | Introduction

Interest surrounding, what are known as "critical minerals," continues to rise due to society's regular technological development and reliance [1]. In recent years, several countries have presented frameworks and made investments toward the development of their critical mineral sectors. For example, in Canada, as is the case for many countries, the federal government is currently investing significant resources into its critical mineral sector, which includes aspects of exploration, extraction, processing, manufacturing, and recycling. A major component of these pillars is the continued advancement of research and technology, which supports the sector. While the term "critical minerals" encompasses over 30 minerals, each has its own importance and target markets in the green and digital economy. Of particular interest to the work presented here is indium and its related compounds, which are ubiquitous in the electronics industry due to their unique properties. With an abundance of only 0.05 ppm in the earth's crust, indium is not found in large mineral deposits, but instead in trace quantities within other minerals deposits [2].

The majority of the world's indium is used to make indium tin oxide (ITO), a transparent semiconductor that can bond to glass. Due to these unique properties, ITO finds applications in modern displays and photovoltaic devices [2, 3]. Indium can be found in a common class of thin film photovoltaic devices that utilize chalcopyrite structured materials as a light-absorbing layer, including copper indium gallium diselenide (CIGSe), copper indium diselenide (CISe), and their sulfide-based variants [4, 5]. Other semiconductors, including indium nitride (InN), indium phosphide (InP), and indium antimonide (InSb), have found use in transistors, microchips, photovoltaics, and other electronic devices. Indium has recently found applications in battery devices, where lithium anodes can be replaced with lithium-indium anodes to suppress perpendicular dendrite formation, avoiding deleterious short circuits and increasing battery stability [6]. Other applications of indium include indium-based catalysts [7, 8], corrosion mitigation [9–11], and various specialized coatings [2]. With increasing demand and limited natural abundance, efforts to recycle indium from used consumer electronics have also gained interest [12–14].

With all of these applications, our ability to characterize interfacial changes is critical to our understanding and future advancements. Few techniques compare to the surface and chemical sensitivity of X-ray photoelectron spectroscopy (XPS), resulting in its widespread use in diverse research fields. For chemical state identification, databases exist including the National Institute of Standard and Technology (NIST) XPS Database [15], the Physical Electronics (PHI) Handbook of XPS [16], and several other online resources (e.g., HarwellXPS.guru, xpsfitting.com, xpsdatabase.com, etc.). Examples of high-quality XPS data can also be found published in *Surface Science Spectra*. While convenient, the use of these databases can be problematic as they often provide information focused only on the main photoelectron signal, can lack consistency in charge referencing, can fail to discuss nuances important to data interpretation, and are sometimes incomplete as they do not provide information for some important compounds.

These limitations can lead to confusion and misinterpretation of data among novice users. Subject experts agree that comprehensive standard data are necessary for researchers to accurately analyze their XPS data [17, 18]. Accordingly, Major et al. have provided an excellent perspective article shedding light on the issues relating to the quality of data interpretation in scientific literature and how we may improve [19]. The analysis of indium and its compounds can often be confusing and prone to misinterpretation due to several factors. One key issue is that the commonly used $3d_{5/2}$ photoelectron line has only subtle shifts in binding energies between various indium species [16]. Additionally, while most trivalent indium species can be modelled using symmetric line shapes, indium oxides have been shown to exhibit more complex peak shapes owing to their electronic properties [20, 21]. These complex shapes are sometimes attributed to separate species without further investigation.

Herein, a comprehensive collection of reference data pertaining to indium and indium-containing compounds is presented. This encompasses various X-ray–induced photoelectron and Auger signals for indium as well as relevant photoelectron signals for the counter-ions. Data include both experimental and literature values. Features that exacerbate fitting procedures, often leading to misinterpretation, such as screening effects and surface modifications are also explored. Tools such as the modified Auger parameter and Wagner plot, which are generally underused in literature, are discussed in the context of single-species datasets. For mixed species systems, the position and shape of the X-ray–induced Auger ($M_{4,5}N_{4,5}N_{4,5}$) signal are highlighted, and an example is given.

2 | Experimental

XPS analyses were carried out using a Kratos AXIS Supra spectrometer (Kratos Analytical, Manchester, UK) using a monochromatic Al Kα source (15 mA, 15 kV, 225 W). The instrument work function was calibrated using metallic gold (i.e., Au $4f_{7/2}$ at 83.96 eV). The spectrometer dispersion was adjusted using metallic copper (i.e., Cu $2p_{3/2}$ at 932.62 eV). During analysis, instrument base pressures were maintained at approximately 10^{-8} to 10^{-9} Torr. All spectra were collected using an analysis area of approximately $300\times700\,\mu m$. Survey and high-resolution spectra were collected with a pass energy of 160 and 20 eV and a step size of 1.0 and 0.1 eV, respectively. For reference, at 20 eV pass energy, a full-width half maximum (FWHM) of approximately 0.55 eV was measured for metallic silver (Ag $3d_{5/2}$).

The Kratos charge neutralizer system was used for analyses as needed. Effective charge neutralization was deemed to have been achieved by monitoring the signal for adventitious carbon (1s). When possible, spectra were charge corrected to give the adventitious C 1s spectral component (i.e., C–C, C–H) a BE of 284.8 eV. The process has an associated error of ±0.1–0.2 eV. A comprehensive discussion on the line shapes expected for adventitious carbon and its use for charge correction can be found elsewhere [22].

All spectra were analyzed using CasaXPS software (version 2.3.23) [17]. Fitting of most spectra was achieved using Gaussian–Lorentzian (GL) product line shapes, defined in CasaXPS as GL(X), where X is the contribution (%) of the Lorentzian function. Please note that the optimal mixture of Gaussian–Lorentzian components will vary depending on the instrument and resolution settings used. Changes to the Gaussian–Lorentzian mix do not, in general, constitute large peak area changes. Reasonable results are obtained when the mix is within a reasonable range and applied consistently. The only exception to the GL(X) line shape was for indium in its metallic state, which was fit considering both Lorentzian asymmetric (LA) and Doniach-Sunjic-Shirley (DSS) line shapes. The LA line shape is defined in CasaXPS as LA(α, β, *m*), where α and β define the spread tail at the high and low B.E. ends of the distribution (respectively), and *m* defines the width of a Gaussian convolution. The DSS line shape is defined in CasaXPS as DS(α, n, l), where α defines the asymmetry parameter, n defines the convolution width, and l defines the influence of the Shirley response to the line shape. More information on these line shapes can be found elsewhere [23]. A standard Shirley background was used for all spectra.

Samples of the highest purity available were purchased from vendors including Alfa Aesar, Thermo Scientific, Millipore Sigma, Delta Technologies, and Princeton Scientific. Where available, samples packaged under inert gas were purchased (e.g., in a sealed glass ampoule). These samples were then introduced into the XPS instrument via an argon glove box attachment. Copper indium disulfide ($CuInS_2$) was synthesized according to the procedures published by Tapley et al. [24].

All powdered samples were mounted on nonconductive adhesive tape. Select samples were cooled using liquid nitrogen during analysis ($InCl_3\cdot4H_2O$, $In(OH)_3$, and InI_3) to avoid their possible decomposition and/or liberation of associated water. For these samples, stage temperatures were maintained between −40°C and −30°C during analyses. Strategies were also employed to limit X-ray exposure for all samples (e.g., minimal scans were taken to obtain sufficient signal-to-noise). No measurable effects of beam damage were found to occur under the analysis conditions employed here. It is also worth noting as a caution that despite these efforts, the analysis of InI_3 led to minor contamination of the analysis chamber, which required subsequent baking to remove.

When possible, selected samples (e.g., In metal, ITO, In_2Te_3, and In_2Se_3) were sputter-cleaned using a gas cluster ionization source (GCIS) to remove surface oxidation. The source was operated using an accelerating voltage of 20 keV and a cluster size of 500 (Ar_{500}^+). For reference, under these operating conditions, the sputter rate through Ta_2O_5 is approximately 2.9 nm min^{-1}.

All samples considered in this study were initially vetted for quality according to the quantification of survey spectra (Table S1). When necessary, samples were also checked for purity using energy-dispersive X-ray spectroscopy (EDX) and/or powder X-ray diffraction (XRD) (Table S2 and Figure S1, respectively). EDX analyses were carried out using a Hitachi SU3900 variable pressure scanning electron microscope combined with an Oxford ULTIM MAX 65 SDD X-ray detector. EDX analyses were carried out using an accelerating voltage of 15 keV. XRD analyses were carried out using a Rigaku SmartLab X-ray diffraction system with Ni-filtered Cu Kα radiation ($\lambda = 1.541862$ Å) in Bragg–Brentano geometry. Diffraction data were acquired over a 2θ range from 5° to 90° with a step width of 0.02° and a scan speed of 3.00° min^{-1}. The ICDD PDF-5+ 2024 inorganic database was used to search for possible phase identification.

Time-of-flight secondary ion mass spectrometry (ToF-SIMS) analyses were conducted utilizing an ION-TOF (GmbH) TOF-SIMS IV system equipped with a BiMn cluster liquid metal ion source. A pulsed 25-keV Bi_3^+ cluster primary ion beam was directed at the sample surface to induce the generation of secondary ions. These secondary ions, either positively or negatively charged, were then extracted from the sample surface across a 300 μm × 300 μm area. Subsequently, they underwent mass separation and detection through a reflectron-type time-of-flight analyzer, enabling simultaneous detection of ion fragments with a mass-to-charge ratio (m/z) of up to approximately 900 within each cycle, which lasted 100 μs. To counteract sample charging, a pulsed, low-energy electron flood was employed. The calibration of positive ion mass spectra was initially accomplished using H^+, CH_3^+, $C_3H_5^+$, and In^+ while negative ion spectra were calibrated using H^-, CH^-, and C_4H^- ions. Sputtering was facilitated by a 3-keV Cs^+ ion beam applied to the surface within a 200 μm × 200 μm area, with ion mass spectra collected over a smaller region (128 μm × 128 μm) within the sputtered area.

3 | Results and Discussion

3.1 | Literature Values

Table 1 presents a collection of average In $3d_{5/2}$ core line binding energies and corresponding standard deviations obtained from published literature. The data from Table 1 are also graphically depicted in Figure 1. These data include and expand upon information presented in the NIST database. For all data, the methods of charge correction were verified and, where possible, corrected to a consistent value of 284.8 eV for the main line of adventitious carbon. Additionally, an attempt was made to vet published data for apparent quality, and data were excluded if experimental problems were identified (e.g., poor sample quality, differential charging, issues related to instrument calibration, etc.). The information provided in Table 1 (and Figure 1) also serves as a method for verifying our experimental data.

TABLE 1 | Average In $3d_{5/2}$ binding energies and their standard deviations obtained from published literature.

Compound	In $3d_{5/2}$ (eV)	Std. dev.	#
In metal	443.7	0.4	19
In_2O_3	444.7	0.4	19
ITO	444.2	0.4	7
$In(OH)_3$	445.2	0.5	7
InF_3	446.4	0.2	3
$InCl_3$	446.2	0.5	4
$InCl_2$	445.5	—	1
InCl	445.1	0.2	2
$InBr_3$	446.3	0.4	4
InBr	445.2	—	1
InI_3	445.7	0.6	3
InI_2	445.1	—	1
InI	444.0	—	1
$In(CH_3COO)_3$	445.4	—	1
$In(C_5H_7O_2)_3$	445.4	—	1
InN	444.1	0.5	8
InP	444.6	0.5	11
InAs	444.3	0.2	3
$InAsO_4$	444.9	—	1
InSb	444.2	0.2	5
In_2S_3	444.9	0.3	7
$CuInS_2$	444.7	0.1	2
In_2Se_3	444.3	0.4	9
InSe	444.3	0.1	3
$CuInSe_2$	444.5	0.4	3
$CuInGaSe_2$	444.4	0.3	3
In_2Te_3	444.4	0.1	2
InTe	444.2	0.4	3

Note: For each compound, the number of citations considered is given (#) [16, 25–87].

The average In $3d_{5/2}$ binding energies obtained from the literature were found to range between approximately 443.7 and

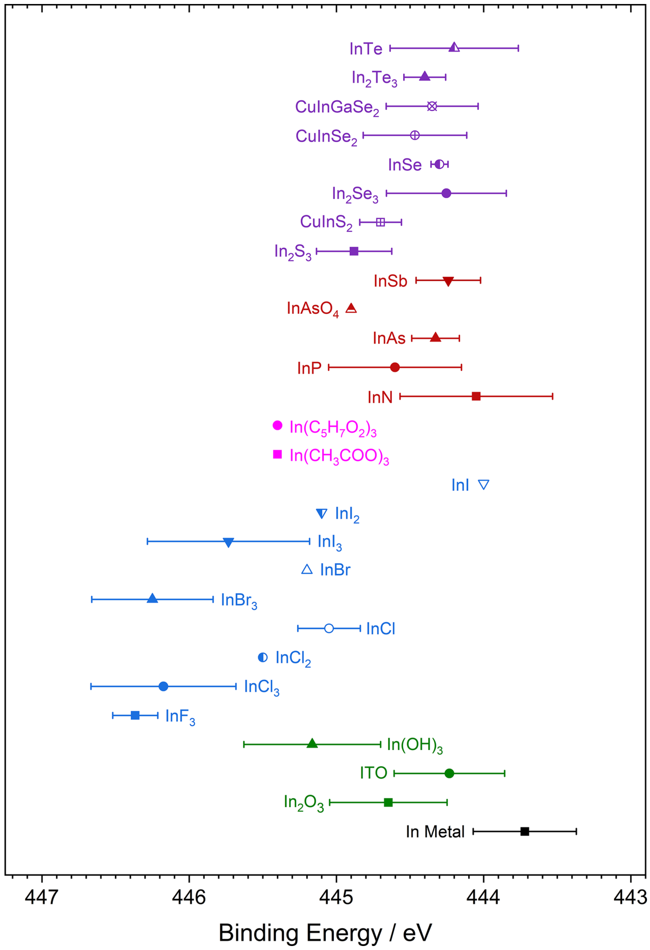

FIGURE 1 | Graphical representation summarizing the average In $3d_{5/2}$ binding energies and their standard deviations obtained from published literature (Table 1). Please note that this representation does not include information relating to peak widths.

446.4 eV with the lowest and highest values found for metallic In and InF_3, respectively. Binding energies of the various pnictogen (N, P, As, and Sb) and chalcogen (O, S, Se, and Te) compounds were found to fall within a relatively narrow energy range (< 1 eV). Binding energies of the halogen (F, Cl, Br, and I) compounds, especially those in which indium is in a trivalent oxidation state, were shifted to higher binding energies relative to the other compounds. As one might expect, the monovalent and divalent indium halides shifted to lower binding energies relative to their trivalent counterparts.

Considering average values in concert with their standard deviations, challenges related to the speciation of various indium compounds become readily apparent. This is then further complicated by factors including natural line widths, line shapes, and errors in charge correction. It is also worth mentioning that our initial literature search included other information—namely the $M_4N_{4,5}N_{4,5}$ line and the corresponding modified Auger parameter. However, we found that the Auger peak was generally underutilized for most indium compounds.

3.2 | Standard Sample Analysis

3.2.1 | Photoelectron Signals

Presented in Figure 2 are the In $3d_{5/2}$ and $3d_{3/2}$ core lines collected for the compounds considered in this study. Table 2 summarizes the average binding energies and standard deviation of the $3d_{5/2}$ line as well as the FWHM and approximate line shapes. Values reported in Table 2 (and subsequent tables) were obtained from replicate measurements, each with a sample size between 3 and 5. In general, the $3d_{5/2}$ and $3d_{3/2}$ core lines were well separated, with an average spin-orbit splitting value of 7.54 (±0.02) eV. The binding energies of the $3d_{5/2}$ line were found to range

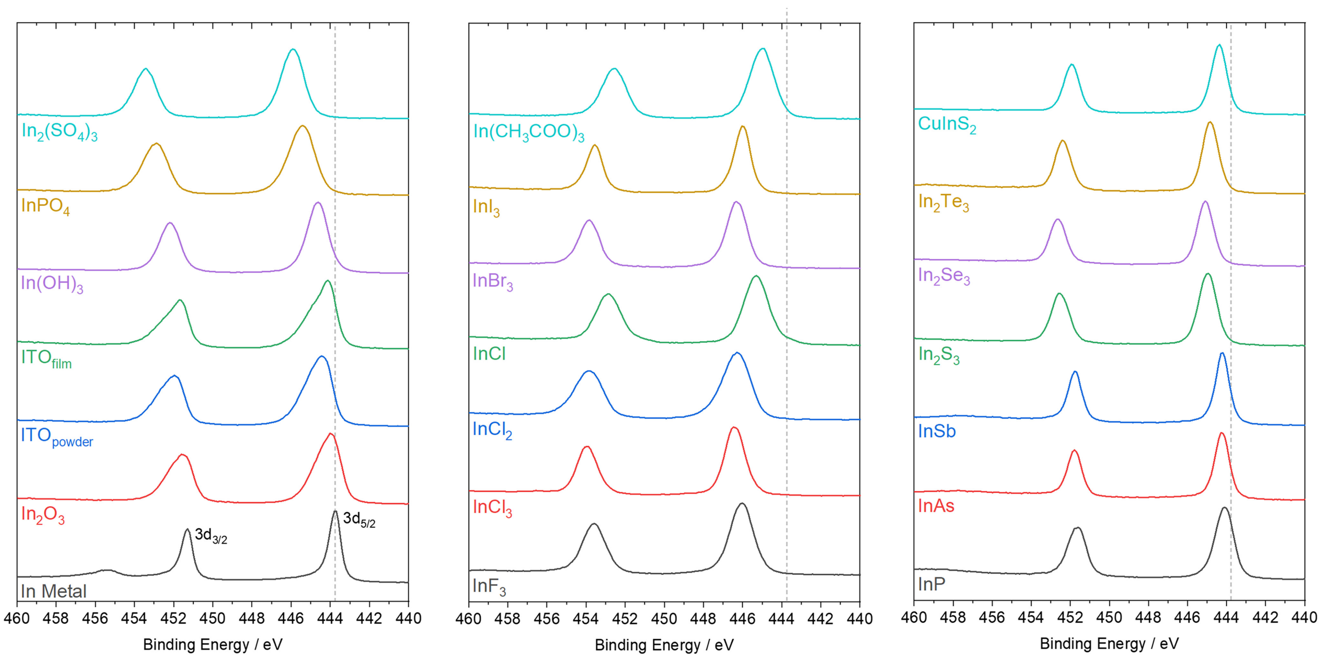

FIGURE 2 | In 3d core line spectra for various indium compounds. For reference, vertical lines indicating the approximate binding energy for metallic indium have been overlaid in each tile.

TABLE 2 | Summary of experimentally measured In $3d_{5/2}$ binding energy, FWHM, and their respective standard deviations.

Compound	In $3d_{5/2}$ (eV)	Std. dev.	FWHM (eV)	Std. dev.	Line shape
In metal	443.8	< 0.1	0.6	< 0.1	LA(0.9, 1.4, 2) DS(0.1,200, 22)
In_2O_3	443.8	0.1	0.9	< 0.1	GL(80)
	444.5	0.1	1.4	< 0.1	
ITO_{Powder}	444.3	0.1	0.8	< 0.1	GL(80)
	445.0	< 0.1	1.4	< 0.1	
ITO_{Film}	444.1	0.2	0.8	< 0.1	GL(80)
	444.9	0.2	1.5	< 0.1	
$In(OH)_3$	444.7	< 0.1	1.3	0.2	GL(65)
$InPO_4$	445.3	0.2	1.4	0.1	GL(65)
$In_2(SO_4)_3$	446.0	0.2	1.3	0.1	GL(75)
InF_3	446.1	0.1	1.5	0.1	GL(70)
$InCl_3$	446.3	0.1	1.2	< 0.1	GL(70)
$InCl_2$	446.2	0.1	1.6	0.1	GL(40)
InCl	445.3	< 0.1	1.4	< 0.1	GL(50)
$InBr_3$	446.3	0.1	1.0	0.1	GL(85)
InI_3	446.0	—	1.0	—	GL(75)
$In(CH_3COO)_3$	445.1	< 0.1	1.4	< 0.1	GL(70)
InP	444.2	< 0.1	0.9	0.1	GL(85)
InAs	444.2	< 0.1	0.8	< 0.1	GL(85)
InSb	444.2	< 0.1	0.8	< 0.1	GL(85)
In_2S_3	444.9	0.1	1.0	< 0.1	GL(75)
In_2Se_3	445.0	0.1	0.9	< 0.1	GL(75)
In_2Te_3	444.8	< 0.1	0.9	< 0.1	GL(70)
$CuInS_2$	444.4	0.1	0.9	0.1	GL(75)

Note: The approximate line shape is provided according to the conventions used in CasaXPS. For In metal, both LA and DS line shapes have been provided.

between approximately 443.8 and 446.1 eV, with extreme values for metallic In and InF_3. This was consistent with our literature review, presented in Table 1. Apart from metallic indium, FWHM values were found to range from approximately 0.8 to 1.7 eV. Notably, the values of FWHM were generally greater for the halides, oxides, and organic compounds when compared to values for the pnictogen and chalcogen compounds. The FWHM of metallic indium (0.55 eV) was less than other compounds, as is common for most metallic elements. Except for metallic indium and the indium oxides, the 3d core lines of all the indium compounds were found to have a symmetrical line shape, which was modelled using variations of the GL line shape.

The line shapes acquired for metallic indium were found to exhibit asymmetry, as is common for metals [88], due to interaction with the conduction band. The $3d_{5/2}$ and $3d_{3/2}$ core lines of metallic indium were modelled using both the LA and DSS line shapes. The $3d_{5/2}$ and $3d_{3/2}$ core lines of metallic indium were also found to exhibit a series of loss structures, shown in Figure 3. Based on the model presented here, three additional components were required for both the $3d_{5/2}$ and $3d_{3/2}$ core lines. For the $3d_{5/2}$ core line, the most prominent loss structure was at approximately 11.7 eV above the main line. This energy loss was found to be consistent with previous reports [38, 44]. Two less intense features were found at approximately 8.5 and 22.8 eV above the main line. For the $3d_{3/2}$ core line, loss features were found to be at similar energies relative to the main line as those found for the $3d_{5/2}$ core line.

The asymmetry of indium oxides did not follow the LA or DSS line shapes used for metallic indium. Instead, a distinct shoulder was observed along the high binding energy side of the main line—suggesting the need for two separate components. In our model, each component fitted a GL(80) line shape. The difference in binding energy between the two components was generally small, on the order of 0.7–0.8 eV. The higher binding energy component was consistently found to have a greater FWHM compared to that of the lower binding energy component.

Notably, the relative size (or area) of these two components was found to vary between samples.

The need for two components appears to have been a source of confusion in recent publications with some researchers mistakenly attributing low and high binding energy components to different oxidation states [89–91] (e.g., In_2O_3 and In metal). Other researchers have rationalized the need for two components as a result of two different surface chemistries originating from the interaction of In_2O_3 with water, forming $In(OH)_3$ and the related oxy-hydroxide species [36, 49, 51]. In the study of the indium oxide interfaces, Donley et al. suggest that asymmetry in the In $3d_{5/2}$ (and O 1s) core line is caused by the formation of a hydroxide and/or oxy-hydroxide species [36]. However, despite heating in an attempt to remove the $In(OH)_3$ from In_2O_3, the authors were not able to completely remove the asymmetry observed in the In 3d core line signals. Similar observations have been made elsewhere [54]. In another study on the surface composition of ITO electrodes, Brumbach et al. described asymmetry for the O 1s, In 3d, and Sn 3d core lines of ITO [49]. The authors attribute asymmetry, at least partially, to a rapid reaction between oxides and water. While their discussion focused mainly on the O 1s core line, they attributed the high binding energy components

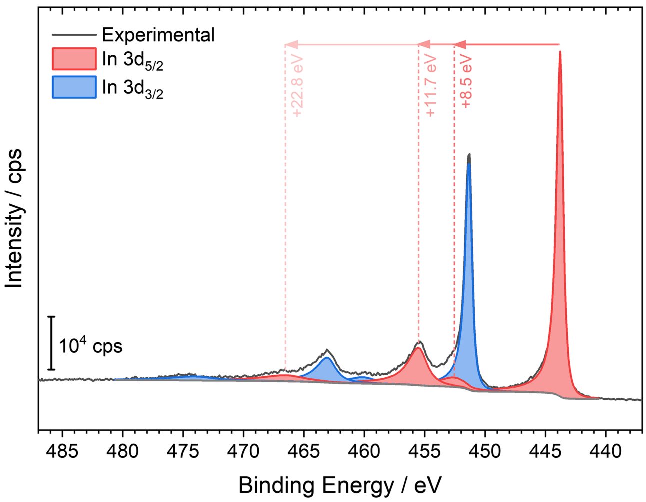

FIGURE 3 | Model of the In 3d core lines for metallic indium showing the corresponding loss structure. The approximate energies for loss features of the $3d_{5/2}$ component are illustrated.

to a hydroxide species. In their study, sputtering the surface was found to reduce the degree of asymmetry (i.e., the size of the high-energy component); however, it could not completely remove the asymmetry. It is worth mentioning that the $3d_{5/2}$ core line measured for $In(OH)_3$ is close in energy to the high-binding energy component detected for various indium oxides (Table 2), suggesting this *may* be a reasonable assignment.

On the other hand, researchers have rationalized the need for two components as a result of the electronic properties of the oxides [20, 21, 50, 53, 92]. More specifically, this has been attributed to screening effects involving the excitation of an electron from the conduction band electrons. Here, two possible final states exist, a screened state where the valence band electron falls into a localized level and an unscreened state where no such transition occurs. This results in signals at lower and higher binding energies, respectively. In a discussion of electronic structure on ITO, Harvey et al. found that asymmetry was stronger for films exhibiting higher conductivity (i.e., higher carrier concentration) [20]. Körber et al. studied the electronic structure of In_2O_3 and ITO in the context of traditional and synchrotron-based hard X-ray photoelectron spectroscopy (HAXPES) [21]. In their work, the higher energy component was generally found to grow in intensity, become broader, and shift to higher binding energies with increasing amounts of Sn-doping. Similar screened/unscreened phenomena have been described for other metal-oxide systems including, but not limited to, Sb-doped SnO_2 [93, 94], RuO_2 [95], IrO_2 [96–98], and MoO_2 [99, 100].

To address the possibility of the first explanation, a surface modification resulting from the interaction with water, angle-resolved XPS (AR-XPS) measurements were made on an ITO_{Film} sample. The resulting In 3d spectra obtained at sample tilts of 0, 15, 30, 45, and 60° are presented in Figure 4A, with 0° being defined as perpendicular to the analyzer. With increases in the sample tilt, no describable difference in the size (area) of the high- and low-binding energy components was observed. In a second set of measurements, a separate ITO_{Film} sample was analyzed before and after fixed sputtered intervals. The resulting In 3d spectra obtained after 0, 100, 200, and 300 s of sputtering are presented in Figure 4B. Similar to AR-XPS measurements, sputtering as much as 300 s revealed no describable difference in the size (area) of the high- and low-binding energy components. Based on the sputter rate obtained for a Ta_2O_5 standard, 300 s

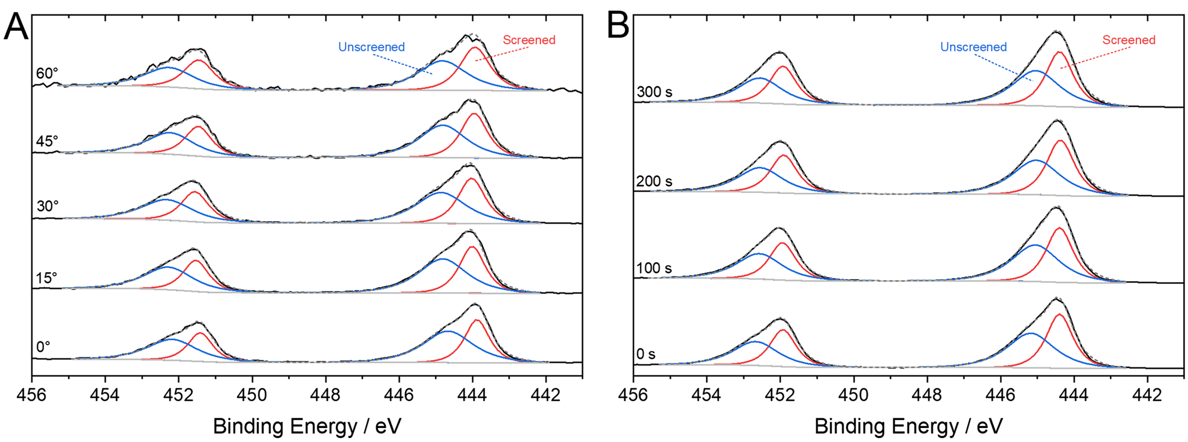

FIGURE 4 | In 3d spectra collected from an ITO_{Film} sample as a function of (A) sample tilt and (B) sputter time (20 keV, Ar_{500}^{+}).

of sputtering under these conditions equates to an approximate depth of 15 nm. This suggests that within the probing depth of XPS (7–10 nm), no chemical changes at the surface region could be detected.

The possibility of a surface modification was also studied by analyzing an additional ITO_{Film} using ToF-SIMS [101]. ToF-SIMS has the advantage of increased surface sensitivity (1–3 nm) when compared to XPS. However, ToF-SIMS is generally a non-quantitative technique with chemical selectivity being obtained through the analysis of molecular ions (either positive or negative) and their relative intensities. A selected mass window collected from ITO_{Powder} and $In(OH)_3$ reference samples and the as-received and sputtered ITO_{Film} surface are presented in Figure S2. By considering the relative intensities of In_2OH^+ and In_2O^+ for ITO_{Powder} and $In(OH)_3$, one finds that for the hydroxide species, the In_2OH^+ ion is more intense compared to the In_2O^+ ion. In contrast, the intensity of In_2O^+ ion is more than In_2OH^+ for ITO_{Powder}. For the as-received surface of the ITO_{Film} sample, the intensity of In_2OH^+ was greater than that of In_2O^+, consistent with the $In(OH)_3$ reference sample. After sputtering, the relative intensities reversed, with In_2O^+ becoming the more intense of the two molecular ions. This change in relative intensities suggests that a small amount of hydroxide *may* be present on the surface of our ITO_{Film} sample. This observation is revisited below in the discussion of mixed systems.

Based on the information available in the literature and the additional experiments presented here, it appears as though the cause of asymmetry is closely tied to the electronic properties of the sample rather than solely a change in surface chemistry. However, it is worth considering that any change in surface chemistry could further complicate interpretation. Especially since the high-binding energy component of indium oxides and indium hydroxide are close in energy. While ToF-SIMS analysis indicated that a small amount of hydroxide *may* be present on the surface of ITO_{Film}, its presence could not be elucidated in our XPS measurements. In conclusion, when present in small quantities, hydroxide may be difficult to distinguish, especially in the case where oxide screening processes play a role in the In 3d signal.

Presented in Table 3 are the average binding energies for the In $3p_{3/2}$ and $4d_{5/2}$ core lines, as well as their standard deviations. Average values of spin-orbit splitting were 37.9 (±0.1) and 0.9 (±0.1) eV for the 3p and 4d core lines, respectively. In general, speciation remains difficult due to only minor shifts in binding energy between the indium compounds considered here. This was similar to the discussion of the $3d_{5/2}$ signal. Notably, the $3p_{3/2}$ signal was found to have relatively large values of FWHM when compared to the $3d_{5/2}$ and $4d_{5/2}$ signals. For the compounds considered in this study, FWHM values for the $3p_{3/2}$ ranged from approximately 3.2 to 3.6 eV. Increased line width complicates the ability to discern subtle shifts in energy. Conversely, the FWHM of the $4d_{5/2}$ signal was found to be narrower, with values ranging from approximately 0.5 to 0.9 eV. While narrower, the $4d_{5/2}$ signal has an increased possibility for spectral overlap, with possible overlaps including potassium (3p), chloride (3s), bromine (4s), iodide (5s), sulfur (3s), and gallium (3d) [16]. Neither the $3p_{3/2}$ nor the $4d_{5/2}$ signals offer additional benefits for speciation compared to the $3d_{5/2}$ signal. However, the ability to select signals based on their inelastic mean free path (IMFP) may be useful, particularly in thin film science. For example, the $3p_{3/2}$ signal may be preferred over the $4d_{5/2}$ and $3d_{5/2}$ signals due to its lower kinetic energy and the resulting decrease in IMFP.

TABLE 3 | Summary of experimentally measured In $3p_{3/2}$ and $4d_{5/2}$ binding energies and standard deviations.

Compound	In $3p_{3/2}$ (eV)	Std. dev.	In $4d_{5/2}$ (eV)	Std. dev.
In metal	665.3	< 0.1	16.7	< 0.1
In_2O_3	665.4	< 0.1	17.2	< 0.1
ITO_{powder}	665.9	< 0.1	17.6	< 0.1
ITO_{film}	665.5	0.1	17.3	0.1
$In(OH)_3$	665.9	< 0.1	17.8	0.1
$InPO_4$	666.6	0.2	18.4	0.1
$In_2(SO_4)_3$	667.2	0.2	19.1	< 0.1
InF_3	667.3	0.1	19.3	< 0.1
$InCl_3$	667.4	0.1	19.5	0.1
$InCl_2$	667.4	0.1	19.2	0.2
InCl	666.5	0.1	18.4	< 0.1
$InBr_3$	667.5	< 0.1	19.3	0.1
InI_3	667.1	—	19.0	—
$In(CH_3COO)_3$	666.1	0.1	18.2	0.1
InP	665.4	< 0.1	17.3	< 0.1
InAs	665.6	< 0.1	17.3	< 0.1
InSb	665.6	< 0.1	17.2	< 0.1
In_2S_3	666.1	< 0.1	18.0	0.1
In_2Se_3	666.3	0.1	18.1	0.1
In_2Te_3	666.2	< 0.1	17.8	< 0.1
$CuInS_2$	665.7	0.1	17.5	< 0.1

Presented in Table 4 are the binding energies and standard deviations relating to the counterions for each compound considered in this study. It is worth mentioning that for the indium oxides, two components were observed in O 1s spectra. Their approximate binding energies were 529.7 and 531.2 eV based on the average of measurements made on In_2O_3, ITO_{Powder}, and ITO_{Film}. Similar observations have been documented for different metal oxide systems [102–106]. The components are generally assigned to a lattice oxide (lower binding energy) and a defective oxide (higher binding energy). These components may also be influenced by the same screening effects observed in the indium core lines [98]. For the samples considered here, the relative area for the defective component varied between 39% and 63% depending on the sample. Generally, the relative area of the higher binding energy component was greater for the ITO samples compared to the In_2O_3 sample. Spectral overlap and the possibility for misinterpretation are found when considering the

TABLE 4 | Summary of experimentally measured binding energy and standard deviation for various counterions.

Compound	Counterion/ core line	Binding energy (eV)	Std. dev.
In_2O_3	O 1s (latt.)	529.5	0.1
	O 1s (def.)	531.2	<0.1
ITO_{powder}	O 1s (latt.)	529.9	<0.1
	O 1s (def.)	531.2	<0.1
	Sn $3d_{5/2}$	486.5	<0.1
ITO_{film}	O 1s (latt.)	529.6	0.1
	O 1s (def.)	531.3	<0.1
	Sn $3d_{5/2}$	486.0	0.1
$In(OH)_3$	O 1s	531.2	0.1
$InPO_4$	P $2p_{3/2}$	133.3	0.1
	O 1s	531.3	0.1
$In_2(SO_4)_3$	S $2p_{3/2}$	169.2	<0.1
	O 1s	532.3	0.1
InF_3	F 1s	685.4	0.1
$InCl_3$	Cl $2p_{3/2}$	199.5	0.1
$InCl_2$	Cl $2p_{3/2}$	199.4	0.1
InCl	Cl $2p_{3/2}$	198.7	0.1
$InBr_3$	Br $3d_{5/2}$	69.6	0.1
InI_3	I $3d_{5/2}$	620.1	—
$In(CH_3COO)_3$	O 1s	531.8	<0.1
InP	P $2p_{3/2}$	128.5	0.1
InAs	As $3d_{5/2}$	40.7	<0.1
InSb	Sb $3d_{5/2}$	527.8	<0.1
In_2S_3	S $2p_{3/2}$	161.5	<0.1
In_2Se_3	Se $3d_{5/2}$	54.3	<0.1
In_2Te_3	Te $3d_{5/2}$	572.9	<0.1
$CuInS_2$	Cu $2p_{3/2}$	932.1	0.3
	S $2p_{3/2}$	161.4	<0.1

approximate binding energy of the defective oxide component for In_2O_3, ITO_{Powder}, and ITO_{Film} (~531.2 eV) and the binding energy of oxygen in $In(OH)_3$ (531.21 eV).

3.2.2 | Auger Electron Signals

Presented in Figure 5 are the In $M_{4,5}N_{4,5}N_{4,5}$ spectra collected for the species considered in this study. Presented in Table 5 are the average kinetic energies and their standard deviations for the $M_4N_{4,5}N_{4,5}$ transition peak maxima. The $M_4N_{4,5}N_{4,5}$ transitions were found to range between approximately 410.5 and 403.9 eV, with extreme values for metallic indium and InF_3, respectively. This trend was consistent with what was found for the In $3d_{5/2}$; however, the spread in energy was greater for the In $M_4N_{4,5}N_{4,5}$ transition ($\Delta_{K.E.} \approx 6.6$ eV) compared to the In $3d_{5/2}$ core line ($\Delta_{B.E.} \approx 2.3$ eV). The modified Auger parameters, as defined by Gaarenstroom and Winograd [107], are also presented in Table 5. Values were found to range between approximately 854.3 and 850.0 eV. Here, it is worth mentioning that the possibility of distinguishing between $In(OH)_3$ and In_2O_3 becomes possible when considering the position and shape of the $M_{4,5}N_{4,5}N_{4,5}$ signal.

3.2.3 | Wagner Plot

Presented in Figure 6 is the Wagner (or chemical state) plot, providing a convenient graphical representation of the $3d_{5/2}$ binding energy (x-axis) and the $M_4N_{4,5}N_{4,5}$ kinetic energy (y-axis). In this representation, the modified Auger parameter is also easily read as the sum of the x- and y-axes, plotted along a 45° diagonal axis. Despite the proven utility of the Wagner plot for speciation and separating initial- and final-state effects [108, 109], it is generally underutilized for indium (and other elements). Inspection of the dataset shown in Figure 6 reveals that similar families of compounds exist in proximity to one another. As an example, the pnictogens, shown in red, are found within a cluster with similar binding energies for the $3d_{5/2}$ and kinetic energies of the $M_4N_{4,5}N_{4,5}$. Similarly, observations are made for the chalcogen (purple), oxide (green), and halide (blue) compounds.

In general, the compounds presented in Figure 6 have a slope of approximately −3 with respect to metallic indium. This is the result of relatively small shifts in binding energy ($3d_{5/2}$) and large shifts in kinetic energy ($M_4N_{4,5}N_{4,5}$). When plotted in this format, a slope of −3 has been shown to suggest that the compounds have similar initial state effects and differing final state effects. A thorough discussion regarding the significance of slope relating to initial and final state effects can be found elsewhere in the work of Moretti et al. [108, 109].

While our literature search found that many researchers rely solely on the In $3d_{5/2}$ core line for chemical speciation, the information presented and discussed above suggests that in most cases, the $3d_{5/2}$ core line alone is not enough to provide conclusive evidence. Even for a "simple" system, that is, one that contains only one chemical species, a proper analysis should include both the $3d_{5/2}$ core line and the $M_4N_{4,5}N_{4,5}$ Auger electron line—at a minimum. When warranted, a comprehensive analysis should also include information relating to the counterion(s) and a discussion on the related stoichiometry.

3.3 | Analysis of Mixed Systems

Identification and quantification of chemical species in a mixed system, that is, one that contains multiple chemical species, becomes increasingly difficult due to spectral overlap. This problem is not unique to indium and has been discussed for several other elements whose main photoelectron signal suffers overlap. For some of these elements, the unique position and shape of the Auger signals have proven useful.

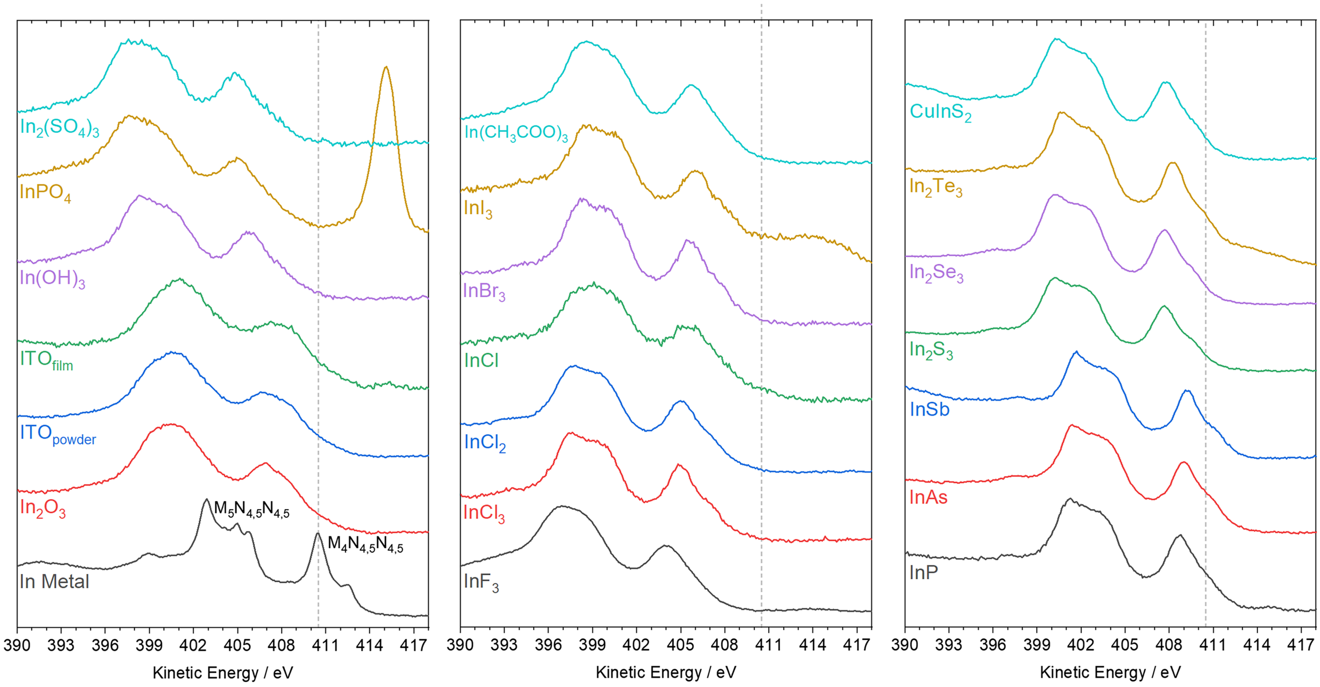

FIGURE 5 | In $M_{4,5}N_{4,5}N_{4,5}$ spectra for various indium compounds. For reference, vertical lines indicating the kinetic energy ($M_4N_{4,5}N_{4,5}$) for metallic indium have been overlaid in each tile. Please note that the additional signal present for $InPO_4$ at 414.7 eV was due to Na contamination.

Some examples include copper [106], nickel [110], gallium [111], and silver [112].

For indium, some researchers have previously utilized the position and shape of the In $M_{4,5}N_{4,5}N_{4,5}$ signal to monitor qualitative changes in the chemical state. Ghaffour et al. used Auger electron spectroscopy (AES) to monitor chemical changes in InP during ion bombardment according to the position and shape of the MNN transition [113]. The authors noted both a shift in kinetic energy and a change in shape, however, they did not quantify changes that were occurring in their study. Similarly, Riegger et al. used the position of the In MNN to characterize chemical changes of indium occurring during the deposition of Li on a Li_3InCl_6 [114]. Again, their analyses were not quantitative, providing only qualitative changes. To the best of our knowledge, the earliest application of the In $M_{4,5}N_{4,5}N_{4,5}$ shape to model a mixed system was provided by Iwasaki et al. during the study of oxidation of InSb [70]. Another example was later provided by Brojerdi et al. in the study of InSe samples undergoing ion beam modification [115]. More recently, Béchu and Fairley presented a detailed discussion on the use of non-linear and linear least squared fitting for the In $M_{4,5}N_{4,5}N_{4,5}$ relating to the oxidation of InSb [116]. The two methods were found to provide similar results with a relative error between 2.1% and 9.2% depending on the dataset. As part of their discussion, the benefit of using the $M_{4,5}N_{4,5}N_{4,5}$ signal over other available photoelectron signals was discussed. The decreased kinetic energy of the $M_{4,5}N_{4,5}N_{4,5}$ signal makes it more surface sensitive when compared to the other available signals.

One of the greatest barriers to the use of the $M_{4,5}N_{4,5}N_{4,5}$ in quantitative analyses is the lack of required information available in the literature. For example, in a number of the publications mentioned above, specifics are provided only for a subset of compounds (e.g., InSb and In_2O_3). Presented in Table 6 are the fitting parameters required to reproduce the $M_{4,5}N_{4,5}N_{4,5}$ envelopes of the compounds considered in this study. Nearly all of the compounds require a total of six individual components to effectively reconstruct the $M_{4,5}N_{4,5}N_{4,5}$ envelope. The exception to this was metallic indium, which required a total of 11 components. It is worth mentioning that while our approach was to use the least number of peaks required, the complexity of the $M_{4,5}N_{4,5}N_{4,5}$ transition for metallic indium could not be adequately reproduced with less.

To effectively utilize these fitting parameters, several considerations must be made. First, background selection is crucial. While various backgrounds are commonly used to model inelastically scattered electrons, the parameters presented here were developed for use with a Shirley background. Deviation from this background is expected to alter peak locations, FWHM values, and relative areas. Second, accurate peak constraints are necessary to avoid significant modification of the synthetic envelope (given by the sum of the individual peaks). Lastly, all available information should be utilized to enhance the accuracy and confidence in the fitting. This includes quantification of the corresponding survey spectrum, information on available counterions, and any supplementary analyses. When employed correctly, this approach to modeling mixed systems has demonstrated its utility. The same methodology has been previously applied to Auger signals [106] as well as photoelectron lines experiencing multiplet splitting [105]. The approximate error associated with this approach can vary, but it is typically considered not to exceed 5%.

TABLE 5 | Summary of experimentally measured In $M_4N_{4,5}N_{4,5}$ kinetic energy, modified Auger parameter ($3d_{5/2}$–$M_4N_{4,5}N_{4,5}$), and corresponding standard deviations.

Compound	In $M_4N_{4,5}N_{4,5}$ (eV)	Std. dev.	Modified Auger parameter (eV)	Std. dev.
In metal	410.5	< 0.1	854.3	< 0.1
In_2O_3	406.9	0.2	850.7	0.2
ITO_{Powder}	406.8	< 0.1	851.1	< 0.1
$ITO_{Thin\ Film}$	407.4	0.3	851.5	0.2
$In(OH)_3$	405.8	< 0.1	850.5	0.1
$InPO_4$	404.7	0.3	850.0	0.1
$In_2(SO_4)_3$	404.7	0.2	850.7	< 0.1
InF_3	403.9	0.1	850.0	0.1
$InCl_3$	404.9	0.2	851.2	0.2
$InCl_2$	405.0	< 0.1	851.2	0.1
InCl	405.4	0.1	850.8	0.1
$InBr_3$	405.6	< 0.1	851.9	< 0.1
InI_3	405.9	—	852.0	—
$In(CH_3COO)_3$	405.6	0.1	850.7	0.1
InP	408.7	< 0.1	852.9	0.1
InAs	409.0	< 0.1	853.3	< 0.1
InSb	409.2	< 0.1	853.4	< 0.1
In_2S_3	407.7	< 0.1	852.6	0.1
In_2Se_3	407.7	< 0.1	852.7	< 0.1
In_2Te_3	408.2	< 0.1	853.0	< 0.1
$CuInS_2$	407.8	< 0.1	852.2	0.1

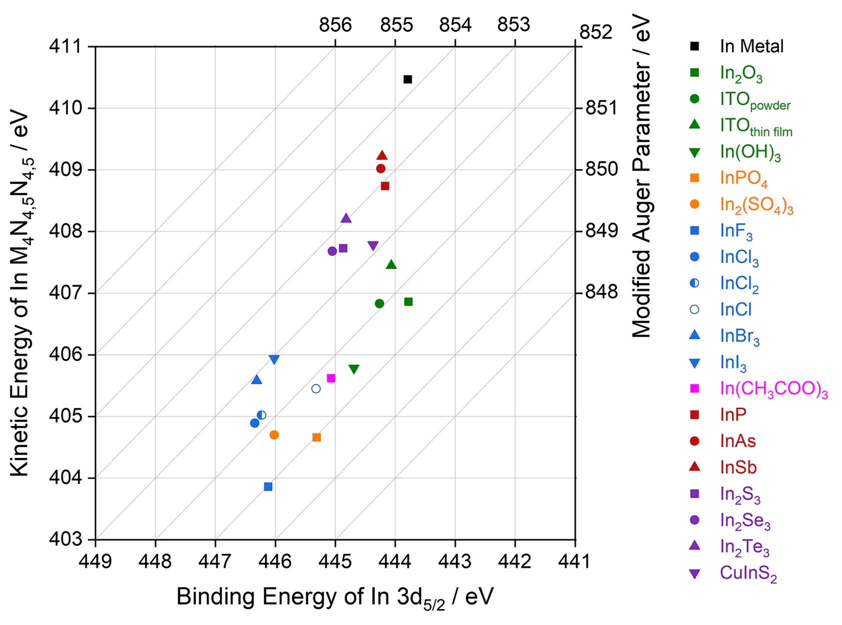

FIGURE 6 | In $3d_{5/2}$–In $M_4N_{4,5}N_{4,5}$ Wagner (or chemical state) plot containing the data obtained for the indium compounds considered as part of this study.

TABLE 6 | In $M_{4,5}N_{4,5}N_{4,5}$ curve fitting parameters.

Compound	Peak 1 (eV)	FWHM (eV)	%	Peak 2 (eV)	Δ peak 2 − peak 1 (eV)	FWHM (eV)	%	Peak 3 (eV)	Δ peak 3 − peak 2 (eV)	FWHM (eV)	%	Peak 4 (eV)	Δ peak 4 − peak 3 (eV)	FWHM (eV)	%	Peak 5 (eV)	Δ peak 5 − peak 4 (eV)	FWHM (eV)	%	Peak 6 (eV)	Δ peak 6 − peak 5 (eV)	FWHM (eV)	%
In_2O_3	410.7	2.5	2.7	407.6	−3.1	4.0	27.8	405.8	−1.8	3.8	7.9	402.0	−3.8	3.8	31.3	399.5	−2.5	3.5	26.4	395.9	−3.6	3.5	3.9
ITO_{Powder}	409.7	3.9	6.8	407.1	−2.6	4.1	30.9	404.0	−3.2	2.9	5.8	401.4	−2.6	3.9	36.1	399.0	−2.4	3.5	18.3	395.2	−3.8	2.7	2.1
ITO_{Film}	410.1	3.6	6.8	407.6	−2.5	4.1	32.5	404.3	−3.2	2.5	6.6	401.8	−2.6	3.6	36.5	399.4	−2.4	3.4	16.0	395.2	−4.1	2.8	1.6
ITO (average)	409.9	3.7	6.8	407.3	−2.5	4.1	31.7	404.1	−3.2	2.7	6.2	401.6	−2.6	3.7	36.3	399.2	−2.4	3.4	17.1	395.2	−4.0	2.8	1.9
$In(OH)_3$	407.6	3.5	15.5	405.9	−1.8	2.1	11.8	404.5	−1.4	2.9	8.0	400.8	−3.8	3.7	36.4	398.2	−2.5	2.6	21.5	395.2	−3.0	3.8	7.1
$InPO_4$	407.3	2.9	6.7	404.9	−2.5	3.0	22.2	401.6	−3.3	3.9	15.9	399.7	−1.9	2.8	15.2	397.5	−2.3	3.3	29.0	394.1	−3.4	5.2	11.0
$In_2(SO_4)_3$	406.8	3.3	13.1	404.7	−2.1	2.4	16.6	402.2	−2.5	3.5	11.5	399.8	−2.4	2.7	21.7	397.4	−2.4	3.1	31.0	393.8	−3.6	3.7	6.1
InF_3	405.2	3.7	17.2	403.7	−1.5	2.5	13.5	401.6	−2.1	2.2	3.4	398.5	−3.1	3.7	36.0	396.3	−2.3	2.7	15.4	393.7	−2.6	5.2	14.6
$InCl_3$	406.4	3.5	19.5	404.9	−1.5	1.6	8.9	403.5	−1.4	3.1	9.7	399.8	−3.8	3.0	32.4	397.4	−2.4	2.3	19.8	395.2	−2.2	5.0	9.7
$InCl_2$	406.3	3.9	22.2	405.0	−1.3	2.0	9.9	403.2	−1.7	3.0	7.3	400.0	−3.2	3.0	28.8	397.6	−2.4	3.0	28.3	393.6	−4.0	2.8	3.5
InCl	407.7	3.6	12.7	405.5	−2.2	2.9	20.1	403.4	−2.1	3.6	6.7	400.2	−3.2	3.7	37.3	397.8	−2.4	2.6	15.3	395.0	−2.8	4.9	8.0
$InBr_3$	406.9	3.4	20.6	405.5	−1.4	1.6	8.5	404.1	−1.5	3.1	9.5	400.4	−3.7	3.0	33.5	398.0	−2.3	2.3	20.6	395.4	−2.7	3.9	7.3
InI_3	408.0	2.1	7.6	406.1	−2.0	2.1	17.9	403.8	−2.2	3.4	10.8	400.7	−3.1	2.8	29.8	398.5	−2.3	2.4	20.2	396.5	−1.9	5.5	13.7
$In(CH_3COO)_3$	407.4	3.8	13.5	405.7	−1.8	2.6	14.9	404.1	−1.6	3.2	5.1	400.2	−3.9	4.1	40.0	397.9	−2.3	2.6	13.5	395.1	−2.8	5.7	13.0
InP	410.3	2.7	15.3	408.7	−1.6	1.7	15.7	407.4	−1.3	2.6	6.0	403.4	−4.0	3.1	38.2	401.1	−2.3	2.1	19.9	398.8	−2.3	4.8	4.9
InAs	410.4	2.8	18.2	409.0	−1.4	1.4	10.3	407.9	−1.1	2.1	6.2	403.6	−4.2	3.4	42.9	401.3	−2.3	2.0	17.5	398.1	−3.2	3.2	5.0
InSb	410.9	2.1	13.7	409.2	−1.7	1.6	20.0	407.5	−1.7	1.8	3.0	404.0	−3.6	2.7	38.3	401.7	−2.3	1.9	22.9	397.9	−3.8	2.7	2.1
In_2S_3	409.0	3.1	19.1	407.6	−1.4	1.5	9.6	406.4	−1.2	3.0	8.0	402.4	−4.0	2.9	36.1	400.1	−2.3	2.2	22.3	397.1	−3.0	3.6	5.0
In_2Se_3	409.8	2.0	7.6	407.8	−2.0	2.1	19.7	407.0	−0.8	5.1	10.0	402.5	−4.5	2.8	33.6	400.1	−2.4	2.3	25.3	396.5	−3.6	2.8	3.7
In_2Te_3	410.1	2.0	10.7	408.3	−1.7	1.6	16.2	406.7	−1.6	3.0	10.2	403.1	−3.6	2.6	31.2	400.8	−2.3	2.2	24.3	398.3	−2.5	4.1	7.6
$CuInS_2$	409.1	3.1	20.3	407.8	−1.3	1.6	9.8	406.6	−1.2	2.8	8.5	402.5	−4.1	3.0	35.9	400.2	−2.3	2.3	23.6	397.2	−3.0	3.0	1.9
In metal	412.3	1.6	5.3	410.5	−1.8	1.2	9.6	409.2	−1.3	4.9	14.8	405.9	−3.4	0.8	2.8	405.0	−0.9	0.5	0.7	404.6	−0.4	3.1	22.6

	Peak 7 (eV)	Δ peak 7 − peak 6 (eV)	FWHM (eV)	%	Peak 8 (eV)	Δ Peak 8 − peak 7 (eV)	FWHM (eV)	%	Peak 9 (eV)	Δ peak 9 − peak 8 (eV)	FWHM (eV)	%	Peak 10 (eV)	Δ peak 10 − peak 9 (eV)	FWHM (eV)	%	Peak 11 (eV)	Δ peak 11 − peak 10 (eV)	FWHM (eV)	%
In metal	402.8	−1.8	1.1	7.1	400.9	−1.9	6.7	26.5	398.8	−2.1	1.1	0.8	392.9	−5.9	5.2	9.2	390.8	−2.0	1.8	0.8

Note: Please note all peak positions are provided in kinetic energy.

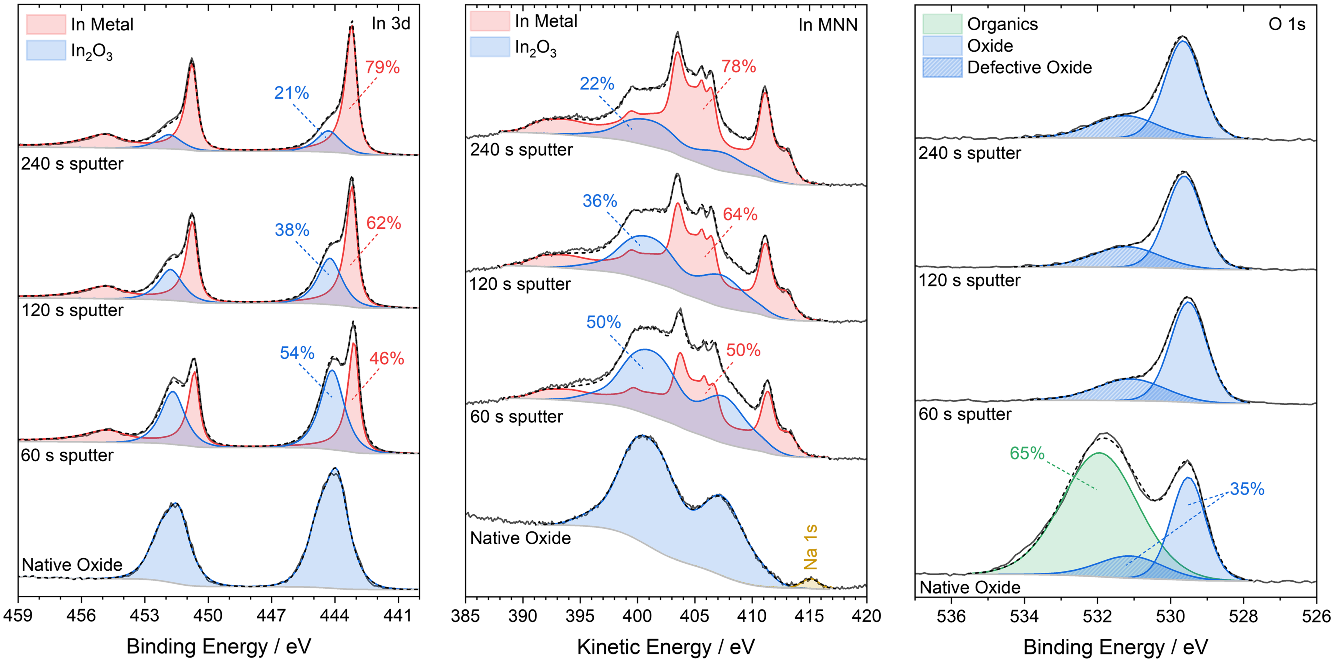

FIGURE 7 | Fitting of In 3d, In $M_{4,5}N_{4,5}N_{4,5}$, and O 1s spectra of selected time points (0, 60, 120, and 240 s) during a depth profile through the native oxide formed on indium metal.

Demonstrating the utility of these fitting procedures, spectra collected at various time points during a depth profile through a native oxide formed on indium foil were considered (Figure 7). However, specifics regarding sample history (e.g., duration, temperatures, relative humidity) are unknown. Therefore, the analysis of this sample serves only as an illustrative example of the application of these fitting parameters.

Based on the quantification of the survey spectrum, the native oxide (or as-received surface) was primarily composed of carbon, oxygen, and indium, with trace amounts of nitrogen, sodium, and calcium. The modified Auger parameter was determined to be 851.0 eV, with the binding energy of the In $3d_{5/2}$ at approximately 444.1 eV and the kinetic energy of the In $M_4N_{4,5}N_{4,5}$ at approximately 406.9 eV. In consideration of standard species, In_2O_3 and $In(OH)_3$ were found to have modified Auger parameters of approximately 850.7 and 850.5 eV, respectively. Notably, the hydroxide species exhibited a lower kinetic energy of the $M_4N_{4,5}N_{4,5}$ (405.8 eV) and slightly higher binding energy of the In $3d_{5/2}$ (444.7 eV) compared to In_2O_3 (406.9 eV and 443.8 eV, respectively).

After considering the similarities between the experimentally measured information and that of the In_2O_3 standard, the dominant species on the as-received surface was determined to be In_2O_3. Subsequently, the In 3d, $M_{4,5}N_{4,5}N_{4,5}$, and O 1s spectra were modelled according to the information provided in Tables 2 and 6, respectively. The results are shown in Figure 7. It is worth noting that while the In 3d signal exhibited slight asymmetry, it was not as pronounced as observed in the standard samples discussed earlier. This difference in asymmetry could be attributed to the electronic properties of the native oxide compared to those of the standard samples, though further investigations would be necessary to confirm this hypothesis. The presence of $In(OH)_3$, at least in detectable quantities, was ruled out due to its inability to fit within the experimental $M_{4,5}N_{4,5}N_{4,5}$ envelope.

In the fitting of the O 1s spectrum obtained from the as-received surface, three components were considered: lattice oxides, defective oxides, and organic species. The amount of organic oxygen was estimated using the relative amounts of C–O, C=O, and O–C=O components in the C 1s spectrum, along with the relative amounts of carbon and oxygen quantified in the survey spectrum (not shown). Further details on this calculation can be found elsewhere [117].

As anticipated, sputtering through the native oxide exhibited a progression from In_2O_3 to metallic indium signals. In the 3d spectra, a signal consistent with metallic indium became evident alongside loss features observed at higher binding energies. Similarly, in the In $M_{4,5}N_{4,5}N_{4,5}$ spectra, features consistent with metallic indium emerged. This transition between the two phases, In_2O_3 and In^0, persisted as sputter times increased. It is worth noting that similar quantifications were obtained for both the In 3d and $M_{4,5}N_{4,5}N_{4,5}$ spectra, despite their differences in kinetic energy (and IMFP). Although this may not be unexpected, the surface of the sample used in this example was not well controlled. Factors such as surface roughness have been shown to increase uncertainty for depth analysis by XPS [118].

In the O 1s spectra, the organic species were completely removed after 60 s of sputtering, uncovering the lattice and defective oxide components. The position and size of these components matched those of the as-received surface, indicating that the two components were independent of sputter intervals.

3.4 | Additional Notes and Considerations

3.4.1 | Monovalent, Divalent, and Trivalent Compounds

Indium compounds are commonly found in the trivalent state, but divalent and monovalent states are also commercially available, particularly for the halides. In our study, we selected and analyzed a series of indium chlorides ($InCl_3$, $InCl_2$, and InCl) to observe changes in binding energy as a function of the oxidation state. We assessed the purity of these compounds by quantifying survey spectra. As expected, the quantification from survey spectra indicated a decrease in chlorine concentration with decreasing oxidation state. Interestingly, the InCl species exhibited a notably higher oxygen concentration compared to $InCl_3$ and $InCl_2$. It is likely that they have varying amounts of surface oxidation in the as-received conditions. For InCl the degree of surface oxidation was higher, possibly owing to its reactivity. Due to the air sensitivity of these compounds, further analysis could not be conducted.

3.4.2 | Surface Modifications

While both In_2Te_3 and In_2Se_3 were purchased with high purities (99.99%), analyses presented here suggest surface stoichiometry differs from the expected 2:3 ratio. When analyzed by XPS (Table S1), elevated amounts of indium were found compared to the respective counter ion (i.e., Te or Se). For In_2Te_3 and In_2Se_3 the ratio of In:X (where X is Te or Se) was 0.9 and 1.2, respectively. When analyzed using EDX, which probes the surface on the order of a few microns, the stoichiometries were consistent with In_2Te_3 and In_2Se_3 (Table S2). For In_2Te_3, XRD analysis was also completed, which showed strong signals for In_2Te_3 and minor peaks for InTe. XRD analysis was not possible for In_2Se_3 due to a strong preferred orientation.

3.4.3 | Valence Band

While valence band analysis was beyond the scope of the discussion presented here, it has been included in the supporting information for reference. Figure S3 presents the corresponding X-ray–induced valence band structure for the compounds considered in the study.

4 | Conclusion

A collection of information relating to indium and various indium-containing compounds has been presented in order to assist researchers in the interpretation of their own XPS data. Reference data for the binding energies photoelectron signals (i.e., In 3d, In 3p, In 4d, and relevant counter ions) as well as the kinetic energy of the X-ray induced In $M_4N_{4,5}N_{4,5}$ are provided. Other diagnostic information including the modified Auger parameter and Wagner (or chemical state) plots have been discussed.

During the discussion of reference data, several key observations were made, summarized below:

- The spread in energy is larger for In $M_4N_{4,5}N_{4,5}$ transition ($\Delta_{K.E.} \approx 6.6\,eV$) compared to the commonly used In $3d_{5/2}$ core line ($\Delta_{B.E.} \approx 2.3\,eV$).
- If asymmetry is observed in the $3d_{5/2}$ core line, screening effects and surface modifications should be taken into consideration and reflected upon.
- It is generally recommended that interpretations include a combination of information obtained from the survey spectra, the In $3d_{5/2}$ core line, the $M_4N_{4,5}N_{4,5}$ transition, the modified Auger parameter, and signals from relevant counterions.
- For modeling mixed systems, leveraging the position and shape of the $M_{4,5}N_{4,5}N_{4,5}$ transition can yield more accurate results than the 3d core line. Using the provided information, a nonlinear least square fitting of the $M_{4,5}N_{4,5}N_{4,5}$ transition can offer quantitative modeling of various indium phases. Additional information such as stoichiometry and further analyses can be incorporated to enhance the accuracy of the fitting process.

Acknowledgments

Financial support was provided by the Natural Science and Engineering Research Council of Canada (Discovery Grant # RGPIN-2022-04475). The Kratos Axis Supra instrument used in this study was provided as part of a Canada Foundation for Innovation (CFI-IF #35961) and Ontario Research Fund. The authors would like to thank Dr. Zhifeng Ding (Department of Chemistry, Western University) for allowing the use of his laboratories and Dr. Matthew Turnbull (Department of Chemistry, Western University) for his assistance in the synthesis of $CuInS_2$. We would also like to thank Dr. Vahid Dehnavi for his assistance with XRD analyses. The authors would also like to acknowledge Mr. Daniel Ovens-Smith (Kratos Analytical, UK) and Mr. Chase McCabe (Kratos Analytical, USA) for their technical assistance and support.

Data Availability Statement

The data that support the findings of this study are available from the corresponding author upon reasonable request.

References

1. Natural Resources Canada. "The Canadian Critical Minerals Strategy," 2022, accessed October 13, 2023, https://www.canada.ca/en/campaign/critical-minerals-in-canada/canadian-critical-minerals-strategy.html.

2. U. Schwarz-Schampera, "Indium," in *Critical Metals Handbook* (Chichester, UK: John Wiley & Sons, Ltd, 2014), 204–229, accessed October 13, 2023, https://onlinelibrary.wiley.com/doi/abs/10.1002/9781118755341.ch9.

3. O. Bierwagen, "Indium Oxide—A Transparent, Wide-Band Gap Semiconductor for (Opto)electronic Applications," *Semiconductor Science and Technology* 30, no. 2 (2015): 024001, https://doi.org/10.1088/0268-1242/30/2/024001.

4. B. Salhi, "The Photovoltaic Cell Based on CIGS: Principles and Technologies," *Materials* 15, no. 5 (2022): 1908, https://doi.org/10.3390/ma15051908.

5. J. P. Sawant, P. K. Bhujbal, N. B. Choure, R. B. Kale, and H. M. Pathan, "Copper Indium Disulfide Thin Films: Electrochemical Deposition and Properties," *ES Materials & Manufacturing* 17, no. 2 (2022): 14–22.

6. S. Luo, Z. Wang, X. Li, et al., "Growth of Lithium-Indium Dendrites in All-Solid-State Lithium-Based Batteries With Sulfide Electrolytes," *Nature Communications* 12, no. 1 (2021): 6968, https://doi.org/10.1038/s41467-021-27311-7.

7. J. Xiong, H. Li, J. Zhou, and J. Di, "Recent Progress of Indium-Based Photocatalysts: Classification, Regulation and Diversified Applications," *Coordination Chemistry Reviews* 473 (2022): 214819, https://doi.org/10.1016/j.ccr.2022.214819.

8. V. Soni, P. Raizada, A. Kumar, et al., "Indium Sulfide-Based Photocatalysts for Hydrogen Production and Water Cleaning: A Review," *Environmental Chemistry Letters* 19, no. 2 (2021): 1065–1095, https://doi.org/10.1007/s10311-020-01148-w.

9. L. Wang, D. Snihirova, M. Deng, et al., "Indium Chloride as an Electrolyte Additive for Primary Aqueous Mg Batteries," *Electrochimica Acta* 373 (2021): 137916, https://doi.org/10.1016/j.electacta.2021.137916.

10. D. Han, S. Wu, S. Zhang, et al., "A Corrosion-Resistant and Dendrite-Free Zinc Metal Anode in Aqueous Systems," *Small* 16, no. 29 (2020): 2001736, https://doi.org/10.1002/smll.202001736.

11. X. Li, M. Liang, H. Zhou, Q. Huang, D. Lv, and W. Li, "Composite of Indium and Polysorbate 20 as Inhibitor for Zinc Corrosion in Alkaline Solution," *Bulletin of the Korean Chemical Society* 33, no. 5 (2012): 1566–1570, https://doi.org/10.5012/bkcs.2012.33.5.1566.

12. F. W. Liu, T. M. Cheng, Y. J. Chen, et al., "High-Yield Recycling and Recovery of Copper, Indium, and Gallium From Waste Copper Indium Gallium Selenide Thin-Film Solar Panels," *Solar Energy Materials & Solar Cells* 241 (2022): 111691, https://doi.org/10.1016/j.solmat.2022.111691.

13. S. Li, Y. Liu, Y. Che, et al., "Recycling of Spent Indium–Gallium–Zinc Oxide Based on Molten Salt Electrolysis," *ACS Sustainable Chemistry & Engineering* 8, no. 43 (2020): 16296–16303, https://doi.org/10.1021/acssuschemeng.0c05986.

14. K. Zhang, Y. Wu, W. Wang, B. Li, Y. Zhang, and T. Zuo, "Recycling Indium From Waste LCDs: A Review," *Resources, Conservation and Recycling* 104 (2015): 276–290, https://doi.org/10.1016/j.resconrec.2015.07.015.

15. A. V. Naumkin, A. Kraut-Vass, S. W. Gaarenstroom, and C. J. Powell, NIST X-Ray Photoelectron Spectroscopy Database (SRD 20), Version 5.0. Published online 1989. https://doi.org/10.18434/T4T88K.

16. J. F. Moulder, W. F. Stickle, P. E. Sobol, and K. D. Bomben, *Handbook of X-Ray Photoelectron Spectrscopy*, ed. J. Chastain (Minnesota, USA: Perkin-Elmer Corporation, Physical Electronics Division, 1992).

17. N. Fairley, V. Fernandez, M. Richard-Plouet, et al., "Systematic and Collaborative Approach to Problem Solving Using X-Ray Photoelectron Spectroscopy," *Applied Surface Science Advances* 5 (2021): 100112, https://doi.org/10.1016/j.apsadv.2021.100112.

18. M. R. Linford, V. S. Smentkowski, J. T. Grant, et al., "Proliferation of Faulty Materials Data Analysis in the Literature," *Microscopy and Microanalysis* 26, no. 1 (2020): 1–2, https://doi.org/10.1017/S1431927619015332.

19. G. H. Major, J. W. Pinder, D. E. Austin, et al., "Perspective on Improving the Quality of Surface and Material Data Analysis in the Scientific Literature With a Focus on X-Ray Photoelectron Spectroscopy (XPS)," *Journal of Vacuum Science and Technology* 41, no. 3 (2023): 038501, https://doi.org/10.1116/6.0002437.

20. S. P. Harvey, T. O. Mason, Y. Gassenbauer, R. Schafranek, and A. Klein, "Surface Versus Bulk Electronic/Defect Structures of Transparent Conducting Oxides: I. Indium Oxide and ITO," *Journal of Physics D: Applied Physics* 39, no. 18 (2006): 3959–3968, https://doi.org/10.1088/0022-3727/39/18/006.

21. C. Körber, V. Krishnakumar, A. Klein, et al., "Electronic Structure of In_2O_3 and Sn-Doped In_2O_3 by Hard X-Ray Photoemission Spectroscopy," *Physical Review B* 81, no. 16 (2010): 165207, https://doi.org/10.1103/PhysRevB.81.165207.

22. M. C. Biesinger, "Accessing the Robustness of Adventitious Carbon for Charge Referencing (Correction) Purposes in XPS Analysis: Insights From a Multi-User Facility Data Review," *Applied Surface Science* 597 (2022): 153681, https://doi.org/10.1016/j.apsusc.2022.153681.

23. B. Moeini, M. R. Linford, N. Fairley, et al., "Definition of a New (Doniach-Sunjic-Shirley) Peak Shape for Fitting Asymmetric Signals Applied to Reduced Graphene Oxide/Graphene Oxide XPS Spectra," *Surface and Interface Analysis* 54, no. 1 (2022): 67–77, https://doi.org/10.1002/sia.7021.

24. A. Tapley, D. Vaccarello, J. Hedges, F. Jia, D. A. Love, and Z. Ding, "Preparation and Characterization of $CuInS_2$ Nanocrystals for Photovoltaic Materials," *Physical Chemistry Chemical Physics* 15, no. 5 (2013): 1431–1436, https://doi.org/10.1039/C2CP42753B.

25. C. J. Powell, "Recommended Auger Parameters for 42 Elemental Solids," *Journal of Electron Spectroscopy and Related Phenomena* 185, no. 1 (2012): 1–3, https://doi.org/10.1016/j.elspec.2011.12.001.

26. R. W. Hewitt and N. Winograd, "Oxidation of Polycrystalline Indium Studied by X-Ray Photoelectron Spectroscopy and Static Secondary Ion Mass Spectroscopy," *Journal of Applied Physics* 51, no. 5 (1980): 2620–2624, https://doi.org/10.1063/1.327991.

27. P. A. Bertrand, "XPS Study of Chemically Etched GaAs and InP," *Journal of Vacuum Science and Technology* 18, no. 1 (1981): 28–33, https://doi.org/10.1116/1.570694.

28. A. K. Tkalich, V. N. Demin, and V. P. Zlomanov, "Oxidation States of In in Pb1-xInxTe," *Journal of Solid State Chemistry* 116 (1995): 33–36.

29. G. Hollinger, R. Skheyta-Kabbani, and M. Gendry, "Oxides on GaAs and InAs Surfaces: An X-Ray-Photoelectron-Spectroscopy Study of Reference Compounds and Thin Oxide Layers," *Physical Review B* 49, no. 16 (1994): 11159–11167, https://doi.org/10.1103/PhysRevB.49.11159.

30. R. G. Copperthwaite, O. A. Kunze, J. Lloyd, J. A. Neely, and W. Tuma, "Surface Analysis of InSb by X-Ray Photoelectron Spectroscopy (XPS)," *Zeitschrift für Naturforschung* 33 (1978): 523–527.

31. L. L. Kazmerski, P. J. Ireland, P. Sheldon, T. L. Chu, S. S. Chu, and C. L. Lin, "Comparison of Low-Temperature Oxides on Polycrystalline InP by AES, SIMS, and XPS," *Journal of Vacuum Science and Technology* 17, no. 5 (1980): 1061–1066, https://doi.org/10.1116/1.570591.

32. G. E. McGuire, G. K. Schweitzer, and T. A. Carlson, "Study of Core Electron Binding Energies in Some Group IIIa, Vb, and VIb Compounds," *Inorganic Chemistry* 12, no. 10 (1973): 2450–2453.

33. D. T. Clark, T. Fok, G. G. Roberts, and R. W. Sykes, "An Investigation by Electron Spectroscopy for Chemical Analysis of Chemical Treatments of the (100) Surface of n-Type InP Epitaxial Layers for Langmuir Film Deposition," *Thin Solid Films* 70, no. 2 (1980): 261–283, https://doi.org/10.1016/0040-6090(80)90367-3.

34. M. Pessa, A. Vuoristo, M. Vulli, et al., "Solid-State Effects in $M_{4,5}N_{4,5}N_{4,5}$ Auger Spectra of Elements From $_{49}$In to $_{52}$Te," *Physical Review B* 20, no. 8 (1979): 3115–3123, https://doi.org/10.1103/PhysRevB.20.3115.

35. R. Nyholm and N. Mårtensson, "Experimental Core-Hole Ground State Energies for the Elements Nb to Te," *Solid State Communications* 40, no. 3 (1981): 311–314, https://doi.org/10.1016/0038-1098(81)90766-3.

36. C. Donley, D. Dunphy, D. Paine, et al., "Characterization of Indium–Tin Oxide Interfaces Using X-Ray Photoelectron Spectroscopy and Redox Processes of a Chemisorbed Probe Molecule: Effect of Surface Pretreatment Conditions," *Langmuir* 18, no. 2 (2002): 450–457, https://doi.org/10.1021/la011101t.

37. X. Tang, R. G. van Welzenis, F. M. van Setten, and A. J. Bosch, "Oxidation of the InSb Surface at Room Temperature," *Semiconductor*

Science and Technology 1, no. 6 (1986): 355–365, https://doi.org/10.1088/0268-1242/1/6/004.

38. A. W. C. Lin, N. R. Armstrong, and K. Theodore, "X-Ray Photoelectron/Auger Electron Spectroscopic Studies of Tin and Indium Metal Foils and Oxides," *Analytical Chemistry* 49, no. 8 (1977): 1228–1235, https://doi.org/10.1021/ac50016a042.

39. C. D. Wagner, "Chemical Shifts of Auger Lines, and the Auger Parameter," *Faraday Discussions of the Chemical Society* 60, no. 0 (1975): 291–300, https://doi.org/10.1039/DC9756000291.

40. M. Ouchene, C. Senemaud, E. Belin, A. Gheorghiu, and M. L. Theye, "Influence of Disorder on the Electronic Distribution of InP by X-Ray and Photoelectron Spectroscopies," *Journal of Non-Crystalline Solids* 59-60 (1983): 625–628, https://doi.org/10.1016/0022-3093(83)90661-0.

41. D. Cahen, P. J. Ireland, L. L. Kazmerski, and F. A. Thiel, "X-Ray Photoelectron and Auger Electron Spectroscopic Analysis of Surface Treatments and Electrochemical Decomposition of $CuInSe_2$ Photoelectrodes," *Journal of Applied Physics* 57, no. 10 (1985): 4761–4771, https://doi.org/10.1063/1.335341.

42. H. Yamaura, T. Jinkawa, J. Tamaki, K. Moriya, N. Miura, and N. Yamazoe, "Indium Oxide-Based Gas Sensor for Selective Detection of CO," *Sensors and Actuators B: Chemical* 36, no. 1 (1996): 325–332, https://doi.org/10.1016/S0925-4005(97)80090-1.

43. P. Sen, M. S. Hegde, and C. N. R. Rao, "Surface Oxidation of Cadmium, Indium, Tin and Antimony by Photoelectron and Auger Spectroscopy," *Applications of Surface Science* 10, no. 1 (1982): 63–74, https://doi.org/10.1016/0378-5963(82)90135-0.

44. Z. M. Detweiler, S. M. Wulfsberg, M. G. Frith, A. B. Bocarsly, and S. L. Bernasek, "The Oxidation and Surface Speciation of Indium and Indium Oxides Exposed to Atmospheric Oxidants," *Surface Science* 648 (2016): 188–195, https://doi.org/10.1016/j.susc.2015.10.026.

45. M. Faur, M. Faur, D. T. Jayne, M. Goradia, and C. Goradia, "XPS Investigation of Anodic Oxides Grown on p-Type InP," *Surface and Interface Analysis* 15, no. 11 (1990): 641–650, https://doi.org/10.1002/sia.740151102.

46. T. L. Barr and Y. L. Liu, "An X-Ray Photoelectron Spectroscopy Study of the Valence Band Structure of Indium Oxides," *Journal of Physics and Chemistry of Solids* 50, no. 7 (1989): 657–664, https://doi.org/10.1016/0022-3697(89)90001-2.

47. Y. A. Teterin, K. I. Maslakov, E. N. Murav'ev, et al., "X-Ray Photoelectron Spectroscopy Study of Indium Tin Mixed Oxides on the Surface of Silicate Glass," *Inorganic Materials* 56, no. 5 (2020): 482–493, https://doi.org/10.1134/S0020168520050131.

48. T. Yan, J. Long, Y. Chen, X. Wang, D. Li, and X. Fu, "Indium Hydroxide: A Highly Active and low Deactivated Catalyst for Photoinduced Oxidation of Benzene," *Comptes Rendus Chimie* 11, no. 1 (2008): 101–106, https://doi.org/10.1016/j.crci.2007.02.012.

49. M. Brumbach, P. A. Veneman, F. S. Marrikar, et al., "Surface Composition and Electrical and Electrochemical Properties of Freshly Deposited and Acid-Etched Indium Tin Oxide Electrodes," *Langmuir* 23, no. 22 (2007): 11089–11099, https://doi.org/10.1021/la701754u.

50. V. Christou, M. Etchells, O. Renault, et al., "High Resolution X-Ray Photoemission Study of Plasma Oxidation of Indium–Tin–Oxide Thin Film Surfaces," *Journal of Applied Physics* 88, no. 9 (2000): 5180–5187, https://doi.org/10.1063/1.1312847.

51. B. Pujilaksono, U. Klement, L. Nyborg, U. Jelvestam, S. Hill, and D. Burgard, "X-Ray Photoelectron Spectroscopy Studies of Indium Tin Oxide Nanocrystalline Powder," *Materials Characterization* 54, no. 1 (2005): 1–7, https://doi.org/10.1016/j.matchar.2004.09.008.

52. Y. Li, G. Zhao, X. Zhi, and T. Zhu, "Microfabrication and Imaging XPS Analysis of ITO Thin Films," *Surface and Interface Analysis* 39 (2007): 756–760.

53. M. Maeng, J. H. Kim, J. A. Hong, and Y. Park, "Effects of Oxygen Plasma Treatments on the Work Function of Indium Tin Oxide Studied by In-Situ Photoelectron Spectroscopy," *Journal of the Korean Physical Society* 68, no. 5 (2016): 692–696, https://doi.org/10.3938/jkps.68.692.

54. J. H. Park, C. Buurma, S. Sivananthan, R. Kodama, W. Gao, and T. A. Gessert, "The Effect of Post-Annealing on Indium Tin Oxide Thin Films by Magnetron Sputtering Method," *Applied Surface Science* 307 (2014): 388–392, https://doi.org/10.1016/j.apsusc.2014.04.042.

55. B. H. Freeland, J. J. Habeeb, and D. G. Tuck, "Coordination Compounds of Indium. Part XXXIII. X-Ray Photoelectron Spectroscopy of Neutral and Anionic Indium Halide Species," *Canadian Journal of Chemistry* 55, no. 9 (1977): 1527–1532, https://doi.org/10.1139/v77-213.

56. Q. X. Guo, M. Nishio, H. Ogawa, A. Wakahara, and A. Yoshida, "Electronic Structure of Indium Nitride Studied by Photoelectron Spectroscopy," *Physical Review B* 58, no. 23 (1998): 15304–15306, https://doi.org/10.1103/PhysRevB.58.15304.

57. Y. H. Chang, Y. S. Lu, Y. L. Hong, C. T. Kuo, S. Gwo, and J. A. Yeh, "Effects of $(NH_4)_2S_x$ Treatment on Indium Nitride Surfaces," *Journal of Applied Physics* 107, no. 4 (2010): 043710, https://doi.org/10.1063/1.3318685.

58. S. Kumar, L. M. L. Mo, M. Motlan, and T. L. T. T. L. Tansley, "Elemental Composition of Reactively Sputtered Indium Nitride Thin Films," *Japanese Journal of Applied Physics* 35, no. 4R (1996): 2261, https://doi.org/10.1143/JJAP.35.2261.

59. J. Zhang, L. Zhang, X. Peng, and X. Wang, "Vapor–Solid Growth Route to Single-Crystalline Indium Nitride Nanowires," *Journal of Materials Chemistry* 12, no. 4 (2002): 802–804, https://doi.org/10.1039/B111270H.

60. B. R. Natarajan, A. H. Eltoukhy, J. E. Greene, and T. L. Barr, "Mechanisms of Reactive Sputtering of Indium I: Growth of InN in Mixed Ar-N2 Discharges," *Thin Solid Films* 69, no. 2 (1980): 201–216, https://doi.org/10.1016/0040-6090(80)90037-1.

61. S. J. Patil, D. S. Bodas, A. B. Mandale, and S. A. Gangal, "Characterization of Indium Nitride Films Deposited by Activated Reactive Evaporation Process," *Thin Solid Films* 444, no. 1 (2003): 52–57, https://doi.org/10.1016/S0040-6090(03)01097-6.

62. Y. Jia, J. S. Wallace, Y. Qin, J. A. Gardella, A. M. Dabiran, and U. Singisetti, "Band Offset Characterization of the Atomic Layer Deposited Aluminum Oxide on m-Plane Indium Nitride," *Journal of Electronic Materials* 45, no. 4 (2016): 2013–2018, https://doi.org/10.1007/s11664-015-4175-9.

63. I. J. Lee, J. Y. Kim, H. J. Shin, and H. K. Kim, "Near-Edge X-Ray Absorption Fine Structure and X-Ray Photoemission Spectroscopy Study of the InN Epilayers on Sapphire (0001) Substrate," *Journal of Applied Physics* 95, no. 10 (2004): 5540–5544, https://doi.org/10.1063/1.1697615.

64. D. M. Poirier and J. H. Weaver, "InP(110) by XPS," *Surface Science Spectra* 2, no. 3 (1993): 256–262, https://doi.org/10.1116/1.1247707.

65. Z. W. Deng, R. W. M. Kwok, W. M. Lau, and L. L. Cao, "InP (110) by Time-Resolved XPS," *Surface Science Spectra* 7, no. 4 (2000): 336–347, https://doi.org/10.1116/1.1379510.

66. Y. Tao, A. Yelon, E. Sacher, Z. H. Lu, and M. J. Graham, "S-Passivated InP (100)-(1×1) Surface Prepared by a Wet Chemical Process," *Applied Physics Letters* 60, no. 21 (1992): 2669–2671, https://doi.org/10.1063/1.106890.

67. R. L. Wells, S. R. Aubuchon, S. S. Kher, M. S. Lube, and P. S. White, "Synthesis of Nanocrystalline Indium Arsenide and Indium Phosphide From Indium (III) Halides and Tris (Trimethylsilyl)pnicogens. Synthesis, Characterization, and Decomposition Behavior of $I_3In{\cdot}(SiMe_3)_3$," *Chemistry of Materials* 7, no. 4 (1995): 793–800, https://doi.org/10.1021/cm00052a027.

68. A. Hofmann, P. Streubel, and A. Meisel, “XPS Investigation of Oxide Films on InP(100),” *Surface and Interface Analysis* 12, no. 5 (1988): 315–319, https://doi.org/10.1002/sia.740120508.

69. W. K. Liu, W. T. Yuen, and R. A. Stradling, “Preparation of InSb Substrates for Molecular Beam Epitaxy,” *Journal of Vacuum Science & Technology, B: Microelectronics and Nanometer Structures-Processing, Measurement, and Phenomena* 13, no. 4 (1995): 1539–1545, https://doi.org/10.1116/1.588184.

70. H. Iwasaki, Y. Mizokawa, R. Nishitani, and S. Nakamura, “X-Ray Photoemission Study of the Initial Oxidation of the Cleaved (110) Surfaces of GaAs, GaP and InSb,” *Surface Science* 86 (1979): 811–818, https://doi.org/10.1016/0039-6028(79)90462-X.

71. M. Afzaal, D. Crouch, and P. O'Brien, “Metal-Organic Chemical Vapor Deposition of Indium Selenide Films Using a Single-Source Precursor,” *Materials Science and Engineering B* 116, no. 3 (2005): 391–394, https://doi.org/10.1016/j.mseb.2004.05.044.

72. P. Liu, S. Yu, W. Fan, and W. Shi, “A New Inorganic–Organic Hybrid In_2Se_3(en) as Hollow Nanospheres: Hydrothermal Synthesis and Near-Infrared Photoluminescence Properties,” *Dalton Transactions* 42, no. 8 (2013): 2887–2893, https://doi.org/10.1039/C2DT32589F.

73. W. Shi, S. Yu, P. Liu, W. Fan, H. Luo, and S. Song, “Near-Infrared Photoluminescent Flowerlike α-In_2Se_3 Nanostructures From a Solvothermal Treatment,” *Chemical Engineering Journal* 225 (2013): 474–480, https://doi.org/10.1016/j.cej.2013.03.066.

74. D. Schmid, M. Ruckh, and H. W. Schock, “Photoemission Studies on Cu (In, Ga)Se_2 Thin Films and Related Binary Selenides,” *Applied Surface Science* 103, no. 4 (1996): 409–429, https://doi.org/10.1016/S0169-4332(96)00099-2.

75. D. Fargues, G. Tyuliev, G. Brojerdi, M. Eddrief, and M. Balkanski, “Ultra-High Vacuum Deposition of Sodium on Indium Monoselenide: Intercalation or Chemical Reaction?” *Surface Science* 370, no. 2 (1997): 201–208, https://doi.org/10.1016/S0039-6028(96)00967-3.

76. Y. Hu, W. Feng, M. Dai, et al., “Temperature-Dependent Growth of Few Layer β-InSe and α-In_2Se_3 Single Crystals for Optoelectronic Device,” *Semiconductor Science and Technology* 33, no. 12 (2018): 125002, https://doi.org/10.1088/1361-6641/aae629.

77. Y. Wang, K. Szökölová, M. Z. M. Nasir, Z. Sofer, and M. Pumera, “Electrochemistry of Layered Semiconducting AIIIBVI Chalcogenides: Indium Monochalcogenides (InS, InSe, InTe),” *ChemCatChem* 11, no. 11 (2019): 2634–2642, https://doi.org/10.1002/cctc.201900449.

78. C. C. Landry and A. R. Barron, “Synthesis of Polycrystalline Chalcopyrite Semiconductors by Microwave Irradiation,” *Science* 260, no. 5114 (1993): 1653–1655, accessed September 29, 2023, https://www.science.org/doi/10.1126/science.260.5114.1653.

79. O. A. Balitskii and W. Jaegermann, “XPS Study of InTe and GaTe Single Crystals Oxidation,” *Materials Chemistry and Physics* 97, no. 1 (2006): 98–101, https://doi.org/10.1016/j.matchemphys.2005.07.055.

80. Z. Yang, J. Guo, H. Li, et al., “Large-Scale Synthesis of Two-Dimensional Indium Telluride Films for Broadband Photodetectors,” *Materials and Design* 233 (2023): 112218, https://doi.org/10.1016/j.matdes.2023.112218.

81. A. Jannat, Q. Yao, A. Zavabeti, et al., “Ordered-Vacancy-Enabled Indium Sulphide Printed in Wafer-Scale With Enhanced Electron Mobility,” *Materials Horizons* 7, no. 3 (2020): 827–834, https://doi.org/10.1039/C9MH01365B.

82. L. Bhira, H. Essaidi, S. Belgacem, et al., “Structural and Photoelectrical Properties of Sprayed β-In_2S_3 Thin Films,” *Physica Status Solidi A* 181, no. 2 (2000): 427–435, https://doi.org/10.1002/1521-396X(200010)181:2<427::AID-PSSA427>3.0.CO;2-P.

83. G. Cao, Y. Zhao, and Z. Wu, “Synthesis and Characterization of In_2S_3 Nanoparticles,” *Journal of Alloys and Compounds* 472, no. 1 (2009): 325–327, https://doi.org/10.1016/j.jallcom.2008.04.047.

84. J. Rodriguez-Pereira, D. A. Miranda Mercado, and R. Ospina, “Indium Acetate Analyzed by XPS,” *Surface Science Spectra* 30, no. 1 (2023): 014013, https://doi.org/10.1116/6.0002596.

85. A. Katerski, A. Mere, V. Kazlauskiene, et al., “Surface Analysis of Spray Deposited Copper Indium Disulfide Films,” *Thin Solid Films* 516, no. 20 (2008): 7110–7115, https://doi.org/10.1016/j.tsf.2007.12.027.

86. G. Teeter, S. P. Harvey, C. L. Perkins, K. Ramanathan, and I. L. Repins, “Comparative Operando XPS Studies of Quasi-Fermi Level Splitting and Open-Circuit Voltage in CZTSe/CdS and CIGS/CdS Junctions and Device Structures,” *Journal of Vacuum Science and Technology* 37, no. 3 (2019): 031202, https://doi.org/10.1116/1.5090345.

87. J. H. Wi, T. G. Kim, J. W. Kim, et al., “Photovoltaic Performance and Interface Behaviors of Cu (In,Ga)Se_2 Solar Cells With a Sputtered-Zn(O,S) Buffer Layer by High-Temperature Annealing,” *Applied Materials & Interfaces* 7, no. 31 (2015): 17425–17432.

88. D. J. Morgan, “XPS Insights: Asymmetric Peak Shapes in XPS,” *Surface and Interface Analysis* 55, no. 8 (2023): 567–571, https://doi.org/10.1002/sia.7215.

89. G. G. Khan, S. Ghosh, A. Sarkar, et al., “Defect Engineered d Ferromagnetism in Tin-Doped Indium Oxide Nanostructures and Nanocrystalline Thin-Films,” *Journal of Applied Physics* 118, no. 7 (2015): 074303, https://doi.org/10.1063/1.4928952.

90. C. Aparna, P. K. Shetty, and M. G. Mahesha, “Investigation on Structural, Optical and Electrical Properties of Zn Doped Indium Oxide Thin Film for Gamma Dosimetry,” *Materials Chemistry and Physics* 302 (2023): 127712, https://doi.org/10.1016/j.matchemphys.2023.127712.

91. T. Huang, C. Mo, M. Cui, et al., “Ion Behavior Impact on ITO Thin Film Fabrication via DC Magnetron Sputtering With External Anode,” *Vacuum* 221 (2024): 112848, https://doi.org/10.1016/j.vacuum.2023.112848.

92. Y. J. Kim, S. B. Jin, S. I. Kim, Y. S. Choi, I. S. Choi, and J. G. Han, “Study on the Electrical Properties of ITO Films Deposited by Facing Target Sputter Deposition,” *Journal of Physics D: Applied Physics* 42, no. 7 (2009): 075412, https://doi.org/10.1088/0022-3727/42/7/075412.

93. F. Borgatti, J. A. Berger, D. Céolin, et al., “Revisiting the Origin of Satellites in Core-Level Photoemission of Transparent Conducting Oxides: The Case of n-Doped SnO_2,” *Physical Review B* 97, no. 15 (2018): 155102, https://doi.org/10.1103/PhysRevB.97.155102.

94. R. G. Egdell, J. Rebane, T. J. Walker, and D. S. L. Law, “Competition Between Initial- and Final-State Effects in Valence- and Core-Level x-Ray Photoemission of Sb-Doped SnO_2,” *Physical Review B* 59, no. 3 (1999): 1792–1799, https://doi.org/10.1103/PhysRevB.59.1792.

95. Y. J. Kim, Y. Gao, and S. A. Chambers, “Core-Level X-Ray Photoelectron Spectra and X-Ray Photoelectron Diffraction of RuO2(110) Grown by Molecular Beam Epitaxy on TiO2(110),” *Applied Surface Science* 120, no. 3-4 (1997): 250–260, https://doi.org/10.1016/S0169-4332(97)00233-X.

96. J. M. Kahk, C. G. Poll, F. E. Oropeza, et al., “Understanding the Electronic Structure of IrO2 Using Hard-X-Ray Photoelectron Spectroscopy and Density-Functional Theory,” *Physical Review Letters* 112, no. 11 (2014): 117601, https://doi.org/10.1103/PhysRevLett.112.117601.

97. V. K. Puthiyapura, M. Mamlouk, S. Pasupathi, B. G. Pollet, and K. Scott, “Physical and Electrochemical Evaluation of ATO Supported IrO_2 Catalyst for Proton Exchange Membrane Water Electrolyser,” *Journal of Power Sources* 269 (2014): 451–460, https://doi.org/10.1016/j.jpowsour.2014.06.078.

98. G. K. Wertheim and H. J. Guggenheim, "Conduction-Electron Screening in Metallic Oxides: IrO_2," *Physical Review B* 22, no. 10 (1980): 4680–4683, https://doi.org/10.1103/PhysRevB.22.4680.

99. J. Baltrusaitis, B. Mendoza-Sanchez, V. Fernandez, et al., "Generalized Molybdenum Oxide Surface Chemical State XPS Determination via Informed Amorphous Sample Model," *Applied Surface Science* 326 (2015): 151–161, https://doi.org/10.1016/j.apsusc.2014.11.077.

100. D. O. Scanlon, G. W. Watson, D. J. Payne, G. R. Atkinson, R. G. Egdell, and D. S. L. Law, "Theoretical and Experimental Study of the Electronic Structures of MoO_3 and MoO_2," *Journal of Physical Chemistry C* 114, no. 10 (2010): 4636–4645, https://doi.org/10.1021/jp9093172.

101. A. Benninghoven, "Chemical Analysis of Inorganic and Organic Surfaces and Thin Films by Static Time-of-Flight Secondary Ion Mass Spectrometry (TOF-SIMS)," *Angewandte Chemie International Edition in English* 33, no. 10 (1994): 1023–1043, https://doi.org/10.1002/anie.199410231.

102. M. C. Biesinger, B. P. Payne, L. W. M. Lau, A. Gerson, and R. S. C. Smart, "X-Ray Photoelectron Spectroscopic Chemical State Quantification of Mixed Nickel Metal, Oxide and Hydroxide Systems," *Surface and Interface Analysis* 41 (2009): 324–332.

103. P. R. Norton, R. L. Tapping, and J. W. Goodale, "A Photoemission Study of the Interaction of Ni(100), (110) and (111) Surfaces With Oxygen," *Surface Science* 65, no. 1 (1977): 13–36, https://doi.org/10.1016/0039-6028(77)90289-8.

104. M. C. Biesinger, L. W. M. Lau, A. R. Gerson, and R. S. C. Smart, "Resolving Surface Chemical States in XPS Analysis of First row Transition Metals, Oxides and Hydroxides: Sc, Ti, V, Cu and Zn," *Applied Surface Science* 257, no. 3 (2010): 887–898, https://doi.org/10.1016/j.apsusc.2010.07.086.

105. M. C. Biesinger, B. P. Payne, A. P. Grosvenor, L. W. M. Lau, A. R. Gerson, and R. S. C. Smart, "Resolving Surface Chemical States in XPS Analysis of First Row Transition Metals, Oxides and Hydroxides: Cr, Mn, Fe, Co and Ni," *Applied Surface Science* 257, no. 7 (2011): 2717–2730, https://doi.org/10.1016/j.apsusc.2010.10.051.

106. M. C. Biesinger, "Advanced Analysis of Copper X-Ray Photoelectron Spectra," *Surface and Interface Analysis* 49, no. 13 (2017): 1325–1334, https://doi.org/10.1002/sia.6239.

107. S. W. Gaarenstroom and N. Winograd, "Initial and Final State Effects in the ESCA Spectra of Cadmium and Silver Oxides," *Journal of Chemical Physics* 67, no. 8 (1977): 3500–3506, https://doi.org/10.1063/1.435347.

108. G. Moretti, "The Wagner Plot and the Auger Parameter as Tools to Separate Initial- and Final-State Contributions in X-Ray Photoemission Spectroscopy," *Surface Science* 618 (2013): 3–11, https://doi.org/10.1016/j.susc.2013.09.009.

109. G. Moretti, "Auger Parameter and Wagner Plot in the Characterization of Chemical States by X-Ray Photoelectron Spectroscopy: A Review," *Journal of Electron Spectroscopy and Related Phenomena* 95, no. 2 (1998): 95–144, https://doi.org/10.1016/S0368-2048(98)00249-7.

110. M. C. Biesinger, L. W. M. Lau, A. R. Gerson, and R. S. C. Smart, "The Role of the Auger Parameter in XPS Studies of Nickel Metal, Halides and Oxides," *Physical Chemistry Chemical Physics* 14, no. 7 (2012): 2434–2442, https://doi.org/10.1039/C2CP22419D.

111. J. L. Bourque, M. C. Biesinger, and K. M. Baines, "Chemical State Determination of Molecular Gallium Compounds Using XPS," *Dalton Transactions* 45, no. 18 (2016): 7678–7696, https://doi.org/10.1039/C6DT00771F.

112. A. M. Ferraria, A. P. Carapeto, and A. M. Botelho do Rego, "X-Ray Photoelectron Spectroscopy: Silver Salts Revisited," *Vacuum* 86, no. 12 (2012): 1988–1991, https://doi.org/10.1016/j.vacuum.2012.05.031.

113. M. Ghaffour, A. Abdellaoui, M. Bouslama, A. Ouerdane, and B. Abidri, "AES, EELS and TRIM Simulation Method Study of InP(100) Subjected to Ar+, He+ and H+ Ions Bombardment," *EPJ Web of Conferences* 29 (2012): 00020, https://doi.org/10.1051/epjconf/20122900020.

114. L. M. Riegger, R. Schlem, J. Sann, W. G. Zeier, and J. Janek, "Lithium-Metal Anode Instability of the Superionic Halide Solid Electrolytes and the Implications for Solid-State Batteries," *Angewandte Chemie, International Edition* 60, no. 12 (2021): 6718–6723, https://doi.org/10.1002/anie.202015238.

115. G. Brojerdi, G. Tyuliev, D. Fargues, M. Eddrief, and M. Balkanski, "Ion Beam Modification of InSe Surfaces," *Surface and Interface Analysis* 25, no. 2 (1997): 111–118, https://doi.org/10.1002/(SICI)1096-9918(199702)25:2<111::AID-SIA215>3.0.CO;2-W.

116. S. Béchu and N. Fairley, "Determination of the X-Auger Electron Spectroscopy Evolution of Indium in InSb by Linear and Nonlinear Least Squares Approaches," *Journal of Vacuum Science and Technology* 42, no. 1 (2024): 013202, https://doi.org/10.1116/6.0003086.

117. B. P. Payne, M. C. Biesinger, and N. S. McIntyre, "X-Ray Photoelectron Spectroscopy Studies of Reactions on Chromium Metal and Chromium Oxide Surfaces," *Journal of Electron Spectroscopy and Related Phenomena* 184, no. 1 (2011): 29–37, https://doi.org/10.1016/j.elspec.2010.12.001.

118. P. L. J. Gunter, O. L. J. Gijzeman, and J. W. Niemantsverdriet, "Surface Roughness Effects in Quantitative XPS: Magic Angle for Determining Overlayer Thickness," *Applied Surface Science* 115, no. 4 (1997): 342–346, https://doi.org/10.1016/S0169-4332(97)00007-X.

Supporting Information

Additional supporting information can be found online in the Supporting Information section.